Daniel Hjelle, BSc

Transmission Electron Microscopy - Electron Energy Loss Spectroscopy Study of Lithium Containing Battery Materials

MASTER'S THESIS

to achieve the university degree of

Diplom-Ingenieur

Master's degree programme: Advanced Materials Science

submitted to

Graz University of Technology

Supervisor

Ao.Univ.-Prof. Dipl.-Ing. Dr.techn. Ferdinand Hofer

Institute for Electron Microscopy and Nanoanalysis

Co-Supervisor:
Dipl.-Ing. Dr. BSc. Georg Haberfehlner

Graz, April 2019

AFFIDAVIT

I declare that I have authored this thesis independently, that I have not used other than the declared sources/resources, and that I have explicitly indicated all material which has been quoted either literally or by content from the sources used. The text document uploaded to TUGRAZonline is identical to the present master‘s thesis.

Date

Signature

Contents

Abstract

Monochromated electron energy loss spectroscopy (EELS) in a transmission electron microscope (TEM) is an excellent technique for the analysis of materials at the nanometer scale, where one can probe the local chemical bonding environments of specific elements. In the present work, a comprehensive monochromated TEM-EELS investigation of the lithium containing materials spodumene, triphylite and lithium vanadium phosphate (LVP) is done, motivated by the importance of lithium-based materials for use in batteries. This is a challenging task due to the radiation damage inflicted on the specimen from the electron beam. Since lithium is a very light element, these materials are likely to experience fast radiation damage; leading to mass loss already after short exposure times. To overcome these challenges, investigations have been performed in cryogenic conditions, cooling the specimens with liquid nitrogen and the experimental procedures have been optimized in order to maximize the spectral quality.

With the optimized procedures, high quality electron energy loss spectra with high energy-resolution (< 0.6 eV) were acquired for all the investigated lithium containing battery materials. The spectra for spodumene, triphylite and LVP are the first to be recorded at this high energy resolution revealing detailed near edge fine structure features for all materials. For triphylite the spectrum is in good agreement with literature, comparing it to artificial $LiFePO_4/LiMnPO_4$. For LVP one can observe the first V $M_{2,3}$ edge for this material recorded in literature. The result obtained for the reference LVP sample also served as reference for comparison to a lithium vanadium phosphate synthesized by a sol-gel method in the presence of carbon (LVP/C). This comparison provided evidence that the crystalline nanowires within the LVP/C sample do not contain vanadium.

Another point that is addressed in the present work is the impact of the two main ionization cross-section models used in EELS on quantification, namely the Hartree-Slater model and the Hydrogenic model. For very light elements, such as lithium or beryllium, quantification performed on EEL spectra in literature has often been poorly explained, and the ionization cross-section models have been chosen without the consideration of the outcome on the final result. In present work, spodumene was used to get an understanding of how these different models affect the quantification of experimental spectra, comparing quantification results for lithium, beryllium and oxygen. From these results it has been found out that there are considerable differences on the values obtained, especially for very light elements like lithium showing differences up to 38 %.

Kurzfassung

Elektronenergieverlustspektroskopie (electron energy-loss spectroscopy/EELS) in einem monochromierten Transmissionselektronenmikroskop (TEM) erlaubt die Untersuchung von chemische Bindungen von spezifischen Elementen in Materialien mit Nanometerauflösung. In dieser Arbeit werden mit TEM-EELS mehrere Lithium-haltige Materialien analysiert: Spodumen, Tryphilin und Lithium-Vanadium-Phosphat (LVP). Lithium-haltige Materialien haben große Bedeutung für den Einsatz in Batterien, die Analyse im TEM ist allerdings auf Grund von Strahlenschädigung eine Herausforderung. Vor allem Lithium, als sehr leichtes Element, ist davon besonders betroffen, daher kann schon eine niedrige Elektronendosis zu Massenverlust führen. Um die Analysen möglich zu machen und Spektren mit hoher Qualität aufnehmen zu können, wurden in dieser Arbeit Untersuchungen unter kryogenischen Bedingungen durchgeführt (Kühlung der Probe mit flüssigem Stickstoff) und experimentelle Parameter optimiert.

Dadurch konnten Energieverlustspektren mit hoher Energieauflösung (< 0.6 eV) für alle untersuchten Lithium-basierten Materialien aufgenommen werden. Die Spektren von Spodumen, Triphilin und LVP wurden damit erstmals bei hoher Energieauflösung aufgnommen, und geben detaillierte Einblicke in die Feinstrukturen der Ionisationskanten für alle enthaltenen Elemente. Das Spektrum von Triphilin ist im Einklang mit Referenzen aus der Literatur für künstliche $LiFePO_4/LiMnPO_4$-Kristalle. Für LVP wurde erstmals die V $M_{2,3}$-Ionisationskante untersucht. Das Spektrum von LVP konnte auch als Referenz verwendet werden, zum Vergleich mit Untersuchungen an Lithium-Vanadium-Phosphat, das in einem Sol-Gel Prozess unter Zugabe von Kohlenstoff hergestellt wurde (LVP/C). Dabei wurde gezeigt, dass kristalline Nanowires, die in der LVP/C Probe vorhanden sind, kein Vanadium enthalten.

Zuletzt wurde der Einfluss der beiden wichtigsten Modelle für den Ionisationsquerschnitt für Elementquantifizierung mit EELS beleuchtet, dem Hartree-Slater Modell und dem Wasserstoffmodell. Für sehr leichte Elemente, wie Lithium oder Beryllium, wurde der Einfluss des gewählten Modells in der Literatur bisher oft nicht ausreichend berücksichtigt. In dieser Arbeit wurde daher die Quantifizierung von Lithium, Beryllium und Sauerstoff in Spodumen mit verschiedenen Modellen verglichen. Diese Ergebnisse zeigen, dass vor allem für sehr leicht Elemente wie Lithium, Variationen bis zu 38 % auftreten.

Acknowledgement

First of all I would like to thank my supervisor Ferdinand Hofer for all his time and support and also for the opportunity to carry out my master thesis at the Institute for Electron Microscopy and Nanoanalysis. I would also thank the Solabat project for the topic for my master thesis.

Special thanks to my co-supervisor Georg Haberfehler for helping me though my thesis including the practical work on the transmission electron microscopes and insightful discussion throughout the time at the FELMI-ZFE.

I would also like to thank Daniel Knez for fruitful discussions regarding beam damage on specimens and Micheala Albu for her time helping me getting a deeper understanding regarding EELS measurements and the transmission electron microscope.

Furthermore I also like to thank Sanja Šimić for the SEM EDX analysis for my materials,
Ilse Letofsky-Papst and Werner Grogger for the discussions regarding beam current measurements.

My specimens would not have been this great without the help from Martina Dienstleder and Sebastian Rauch. So I would also like to thank them for helping me with specimen preparation and discussion around this.

I would also like to thank Margit Wallner for top quality photos that were taken of the minerals.

The students at the Diplomatenzimmer must not be forgotten, I would like to thank all of them for a pleasant working environment with a lot of funny discussions and our dinner and game nights.

I would also like to thank everyone else at the FELMI-ZFE for making my stay here a pleasure.

At last I would like to thank my parents and friends back in Norway for their support and patience.

Introduction

Lithium containing materials are important for e.g energy materials like Li-ion batteries and are as shown in figure 1, getting more attention by the scientific world and therefore one needs to investigate these materials further. This is mainly due to the ever-increasing energy demands of the growing population and that this energy has to come from renewable resources. The aim is to make the best use of this energy and therefore proper energy storage systems like Li-ion batteries are needed. For these further developments, reliable methods for analyzing lihium at high lateral resolution are necessary.

There are number of techniques for detecting and quantifying light elements like lithium, particularly those which involve using the transmission electron microscopy (TEM) and this is due to their high spatial resolution.

Energy-dispersive X-ray spectroscopy (EDX) in scanning electron microscopy (SEM) may be one of the most popular analytical techniques but due to strong absorption of light elements by the surface layers and surrounding heavier elements, it is not possible to detect lighter elements than boron. Other techniques are high-resolution transmission electron microscopy (HR-TEM) and scanning transmission electron microscopy (STEM). These techniques are a good way to indirectly observe lithium but with these techniques it is not possible to probe the local chemical bonding environments for investigated elements on the specimen [39]. A promising technique, however, is electron energy-loss spectroscopy (EELS), which is the only method for analyzing lithium in materials at a high lateral resolution down to nanometer resolution [25]. With EELS it is possible to probe the local chemical bonding environments of specific elements on the specimen and it is a very effective technique for light elements like lithium.

There are however challenges regarding the detection of lithium and to measure the lithium concentration using this technique [25]. The electron beam produced by the TEM introduces radiation damage to the specimen which will lead to a loss of lithium and also crystallinity over time. The ionization edge of lithium lies within the low-loss region, where one can expect a high signal but as a consequence of this, also a very low signal-to-background ratio. Quantitative analysis of lithium can be very challenging due to overlapping edges from different elements from, for example, the first row of transition metals or from the L edges of lighter elements like silicon.

In this thesis, we will work with a monochromated TEM-EELS system to get a deeper understanding of three selected lithium-containing battery materials. Spodumene will be a test sample for quantification and show the consequences of radiation damage, triphylite will be a test sample for lithium containing phosphates and lastly two lithium vanadium phosphates will be compared which were synthesized by colleagues from the SOLABAT project using two different sol-gel methods [27][55].

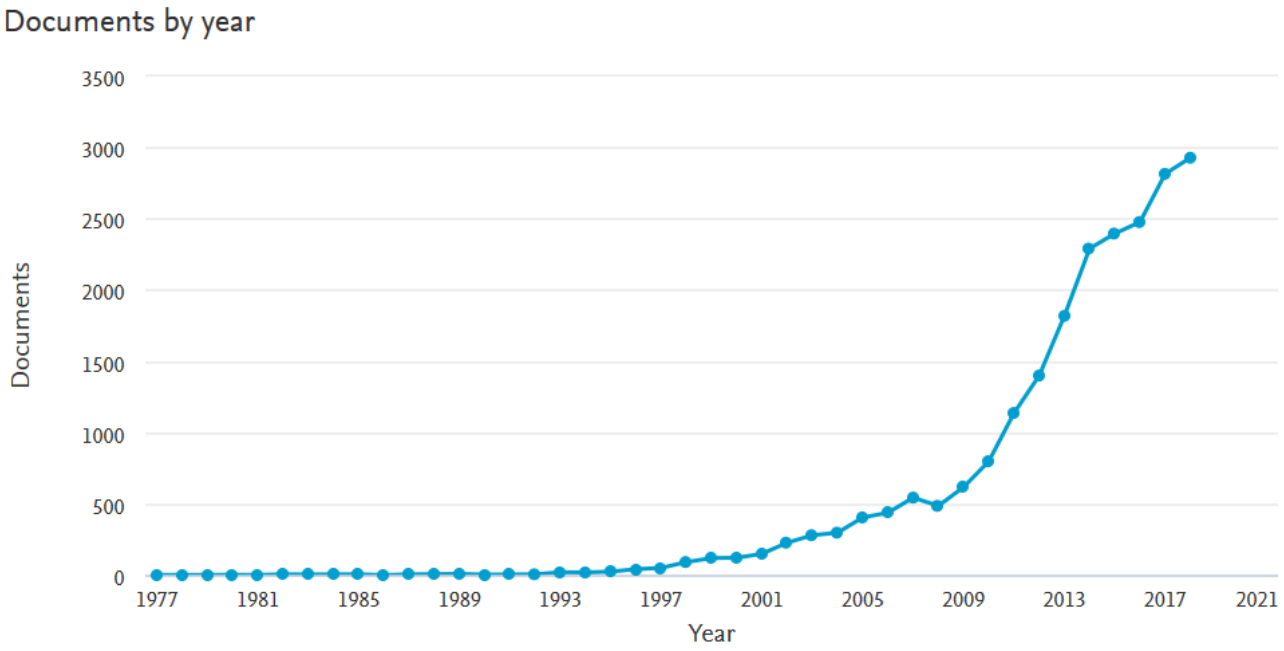

Figure 1: Historical chart showing academic publications with the keyword "Li-ion batteries" from 1977 up to and including 2018 (www.scorpus.com).

Chapter 1

Theory

1.1 Basics of transmission electron microscope

The transmission electron microscope (TEM), which was built and designed by Ruska and Knoll in the 1930s, is a good analytical tool within material science which can be used to visualize and analyze specimens all the way down to atomic resolution. A typical schematics of a conventional TEM can be seen in figure 1.1.

1.1.1 Electron sources

The electron source producing the incident beam can either be a filament that is made of a material that has a low work function, typically tungsten or a ceramic material such as lanthanum hexaboride (LaB_6) and a focusing electrode (Wehnelt). This filament works on the principle of thermionic emission which means that thermal energy is given to the carrier to overcome the work function of the material and when this is the case, electrons leak out and can be accelerated.

The other electron source can be a field emission gun (FEG), which is not as in the filaments case, a thermal filament, but instead an electric field is applied and increased at the tip. The consequence of this is that the electrons can tunnel out and be accelerated. In both types of electron guns the electron beam that is produced by accelerating the electrons is then accelerated towards an anode with typically a total energy of between 100 and 300 keV.

1.1.2 Electron-optical coloumn

The working principle of TEM [14] can be divided into three parts, the illumination system, the objective lens region and the imaging system. The illumination system is where the electron beam is demagnified by at least two electromagnetic condensers (C1 and C2) all the way down to a few ångström. One lens (C1) forms a demagnified image of the gun crossover while another lens (C2) is adjusting the illumination mode to become either parallel or convergent.

The objective system is where the main electromagnetic objective lens forms both the first intermediate, real-space projection image of the illuminated specimen area and also the corresponding

reciprocal space diffraction pattern. For the imaging system an objective aperture can be introduced to limit beam divergence in reciprocal space of the transmitted electrons that contribute to the magnified image. Before the electron fluorescent microscope viewing screen, one can find the projector lens system that consists of an intermediate lens that focus on the objective lens image plane or the back focal plane. This lens is followed by a series of up to four further projector lenses that can give a magnification of up to one million times.

The TEM can be operated in two operation modes:

Imaging mode

Within imaging mode one can either acquire bright field (BF) images or dark field (DF) images. The BF images are generated by the primary beam while DF images are generated by blocking the primary beam and only pass through scattered electrons to form the image.

Electron diffraction mode

Electron diffraction can be achieved by either, when a specimen is illuminated by a parallel beam, inserting a selected area electron diffraction aperture (SAED). This aperture is located in the plane of the first intermediate image and defines the region where the diffraction is obtained. Or by a convergent beam electron diffraction (CBED), focusing the beam on a specimen and form a small convergent probe. This technique form the diffraction pattern as discs and not points which can give information about crystal symmetry of the investigated specimen.

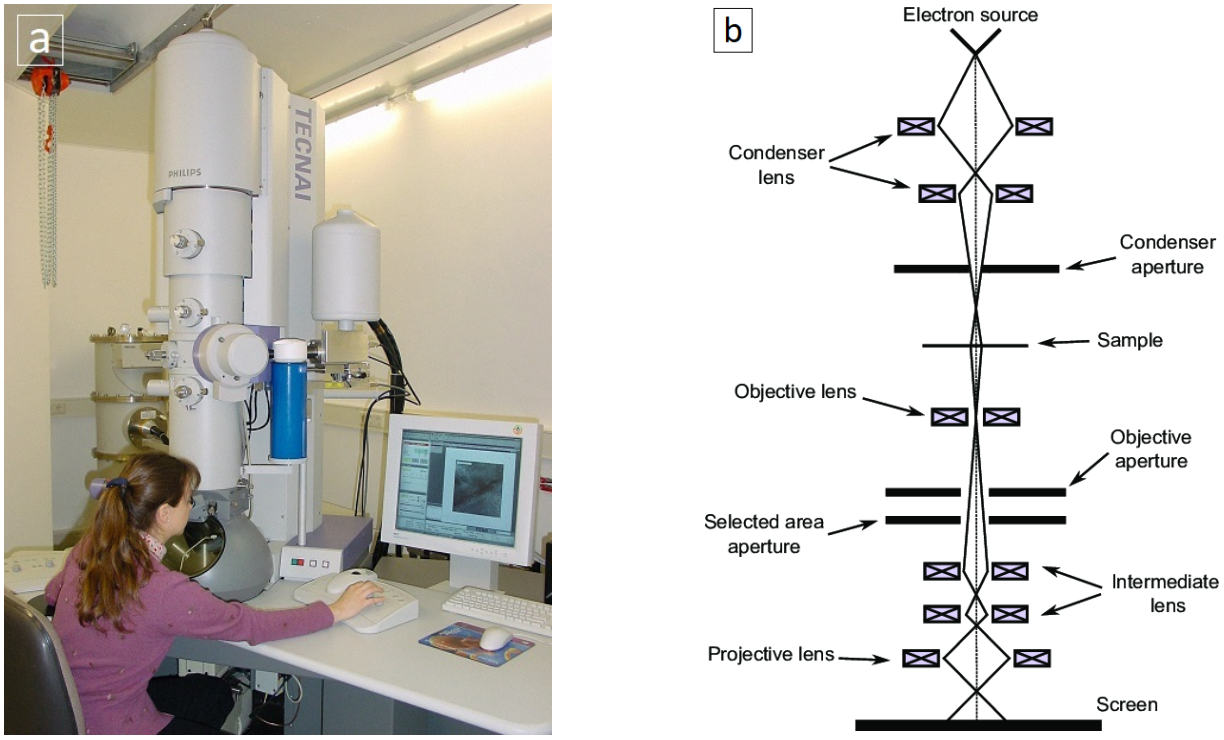

Figure 1.1: (a) FEI Tecnai G2 TF20 (by M. Wallner) (b) basic schematics of a TEM [36].

1.1.3 Electron/matter Interaction

Since the basis of the TEM is an electron beam that interacts with the specimen, one has to look more closely into what can happen when electrons interact with matter. An general illustration of the different interactions that can occur when electrons interact with matter can be seen in figure 1.2. From these interactions it is possible to gain insights into the structure, morphology and composition of the material [14].

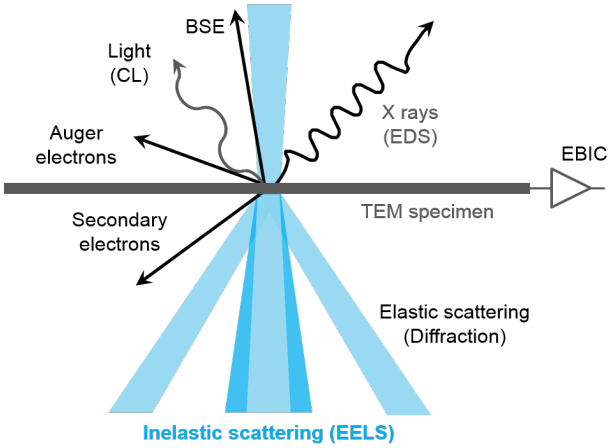

Figure 1.2: Overview of scattering processes [5]

In TEM, all contrast is based on scattering of electrons in the specimen. These scattering processes can be distinguished between inelastic or elastic scattering. Elastic scattering is an interaction that occurs when there is no change in energy of the primary electron but there might be large changes in direction. Within elastic scattering, there are two basic types of events: Large-angle elastic scattering (angle greater than 5 degrees), which is also known as Rutherford scattering, and small-angle elastic scattering (angle less than 5 degrees, typically 10 - 100 milliradians). This occurs when electrons travel much farther from the nucleus and arises from the scattering of the incident electron by the screened nuclear field, the screening arising from the electron cloud of the atom. Elastically scattered electrons are the main contribution to diffraction patterns and images [14].

Inelastic scattering on the other hand, there is a loss of energy of the primary electron. It is this energy-loss that forms the basis of electron energy loss spectroscopy (EELS) [14].

Several processes are responsible for energy-losses and the most important are [14]:

- Phonon excitation - Primary electron excites phonons due to atomic vibrations in the solid. The energy loss from this is <0.2 eV.
- Plasmon and valence excitations - Primary electron excites collective, "resonant" oscillations of the valence electrons in a solid. Expected energy loss from this is within the range 1-30 eV.
- Single electron excitation - the primary electron transfers some of its energy to a single electron in the material resulting in ionization.
- Direct radiation losses - Fast incident electrons can also loose energy in solids due to deceleration processes in which energy is emitted directly in the form of photons.

1.1.4 Beam damage

Beam damage can be described as "Once its structure or chemistry is changed, your thin specimen is not representative of its parent material and interpreting any of your TEM images, DPs or spectra becomes more difficult." [52]. All materials can virtually be damaged when analyzed with a TEM and especially lithium containing materials (this will be shown later in this thesis). This beam damage is therefore represented as a real physical limit on what the TEM can do. Damage is represented within three principal forms [52]:

- Radiolysis - Inelastic scattering breaking the chemical bonds of certain materials. One can for example find this kind of beam damage in polymers and alkali halides
- Knock-on damage / sputtering - Displacement of atoms from crystal lattice and the creation point defects or atoms ejected from specimen surface. These effects will occur when the beam energy is higher than the threshold energy of the specific material which is often the case in TEM.
- Heating - Phonons heat up the specimen and this heat is an important source of damage especially to polymers and biological tissue.

For the case of light elements like lithium, beryllium and boron, the beam damage occurs most likely from radiolysis but also displacement damage. This is because the incident-beam threshold energy is normally below 20 keV [20].

There are a few ways to reduce the effect of beam damage or at least slow down this effect. The specimen can be cooled down using for example liquid nitrogen. Use higher voltages (but this again can increase the chance of knock-on and sputtering damage) and thinner specimens. If the specimen is very thin, then most electrons will just go through the specimen and therefore less energy is transferred to the specimen which again results in less damage due to heating effects [52].

1.1.5 Electron energy loss spectroscopy

Electron energy loss spectroscopy (EELS) is an important analytical tool for the characterization of materials by recording the energy distribution of electrons that pass though the specimen. An EEL spectrum is typically separated into three regions [32].

- Zero loss peak (ZLP) - The ZLP is formed by electrons that have not lost any energy (or less than resolution of the spectrum). If the specimen is thin, this peak is by far the most intense one.
- Low loss region - Electrons that have interacted with weakly bound electrons in the specimen and the plasmon peaks are the predominant feature.
- Core loss region - Electrons that have interacted with core electrons of the atom. Illustration of the classification of core transitions that occur in EELS can be seen in figure 1.3. These core - level excitations lead to edge-like features with an onset energy corresponding to the difference between the energy of the bound electrons.

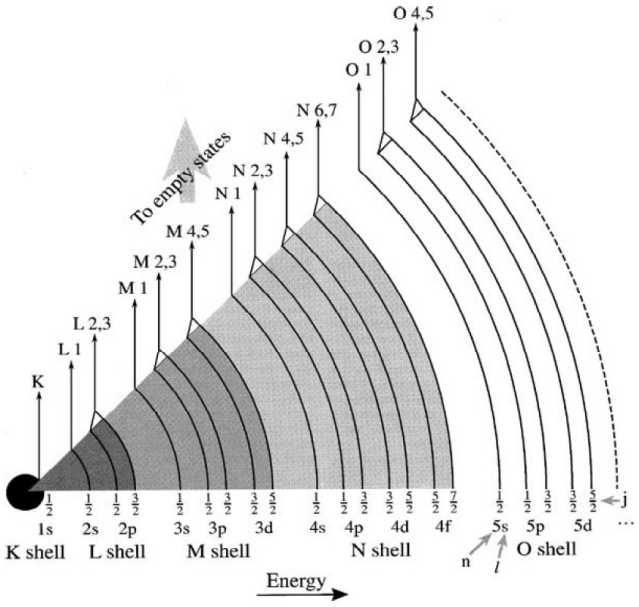

Figure 1.3: Classification of core transitions in EELS [52].

An illustration of these regions can be seen in figure 1.4 which is taken from a holey carbon grid.

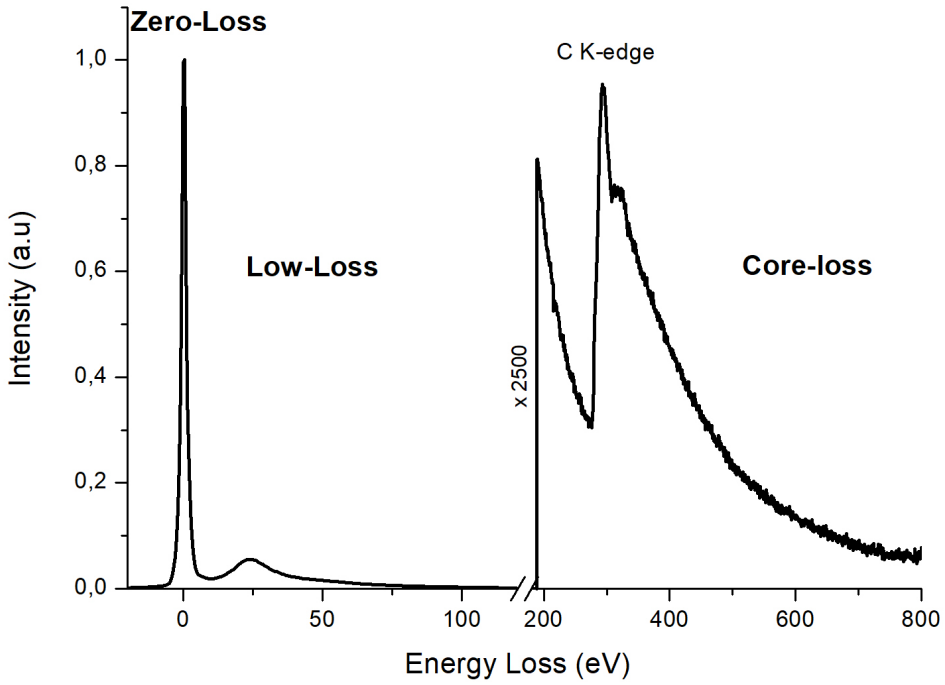

Figure 1.4: Illustration of an EEL spectrum taken on a holey carbon grid including the three typical regions.

Effective and ideal collection angle

The main angles (i.e. semi-angles) in TEM can be seen in figure 1.5. The convergence angle α is the semi-angle of the cone shaped electron beam that illuminates the specimen and in TEM-mode (parallel illumination), this angle is normally close to zero. This angle is determined by condenser lens and aperture. The collection angle β is determined by the objective aperture, the spectrometer aperture, the camera length and also the mechanical specification of the used instrument[2].

For accurate determination the of partial cross-section, which is used for quantification, the effective collection angle β^* have to be known. The collection angle β is equal to the effective collection angle β^* if $\beta > \alpha$. There is however another aspect one has to consider. If the collection angle β is increased, the signal to noise ratio (SNR) also increases but if β becomes too large, the signal to background ratio (SBR) decreases. One therefore needs to find the ideal collection angle β for the different elements that will be investigated. This ideal collection angle can be found by first finding the characteristic scattering angle Θ_E and this can be found by using formula 1.1.

The recommended collection angle is 3 x Θ_E to optimize SBR[10]. The calculated Θ_E and the recommended collection angle β can be found in table 1.1

$$\Theta_E = \frac{E}{2E_o} \tag{1.1}$$

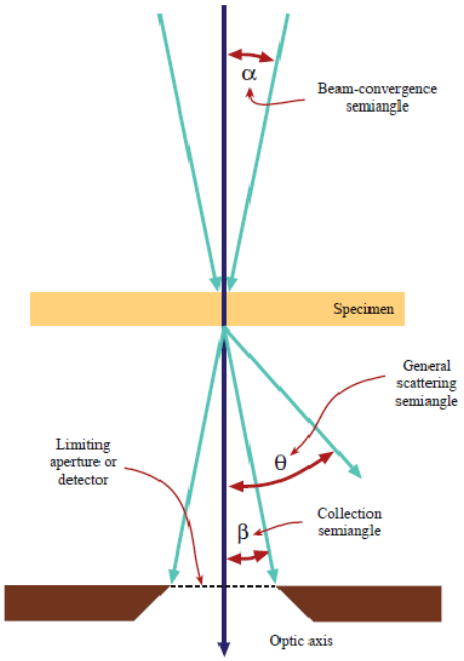

Figure 1.5: Schematics of the main angles in TEM. Showing convergence angle α and collection angle β [52].

Table 1.1: Calculated characteristic scattering angles for the different ionization edges to analyze the materials of this thesis (200keV).

E_o = 200 keV	V $M_{2,3}$	Mn $M_{2,3}$	Fe $M_{2,3}$	Li K	Al $L_{2,3}$	Si $L_{2,3}$	P $L_{2,3}$	O K
$\Delta E \geq (eV)$	38	49	54	55	73	99	132	532
ΘE (mrad)	0.095	0.123	0.135	0.138	0.183	0.248	0.330	1.33
3ΘE (mrad)	0.285	0.369	0.405	0.413	0.546	0.743	0.990	3.99

Specimen thickness

The most common method to measure the specimen thickness within a region, where the region is defined either by the incident beam or an area-selecting aperture, is called the log-ratio method. This method requires you to record a low-loss spectrum and then compare the area I_0 under the zero-loss peak with the total area I_t under the whole spectrum. The relative thickness t/λ, where t is the thickness and λ is the total mean free path for all inelastic scattering, can from this be calculated using equation 1.2 [8]. In this equation, the determination of λ is difficult and therefore the accuracy (if calculated values) is limited.

$$t/\lambda = -ln(I_t/I_0) \tag{1.2}$$

This method is implemented in the Gatan EELS software and by using the "compute thickness" procedure the relative thickness of the investigated specimen can easily be determined. Note: If the instrument used have a collection aperture that limit the scattering angle Θ which is recorded by the spectrometer, then λ should rather be interpreted as an effective mean free path which is dependent on the angle Θ ($\lambda(\Theta)$). Low-loss EEL spectrum was taken from two specimens with different thickness shown in figure 1.6. Using the "compute thickness" process in the Gatan EELS software it was found out that the relative thickness of the specimen resulting in the EEL spectrum on the left, was 0.2 t/λ and on the right, the value was 2.5 t/λ. This figure is an illustration how the low-loss EEL spectrum changes with thickness and also where the intensity regions are for I_0 and I_t.

I_0 integral should start somewhere on the left of the ZLP to the first minimum after the peak of the ZLP. I_t integral starts at the same location as the I_0 integral and be integrated to an energy-loss value that corresponds to a value which is high enough that further increase if energy window Δ will not affect the accuracy. For thin specimens this integral energy window does not need to be higher than Δ = 100 eV but one need to consider a longer Δ if thicker specimens (or specimens with high Z value) are examined, for accurate thickness determination [20].

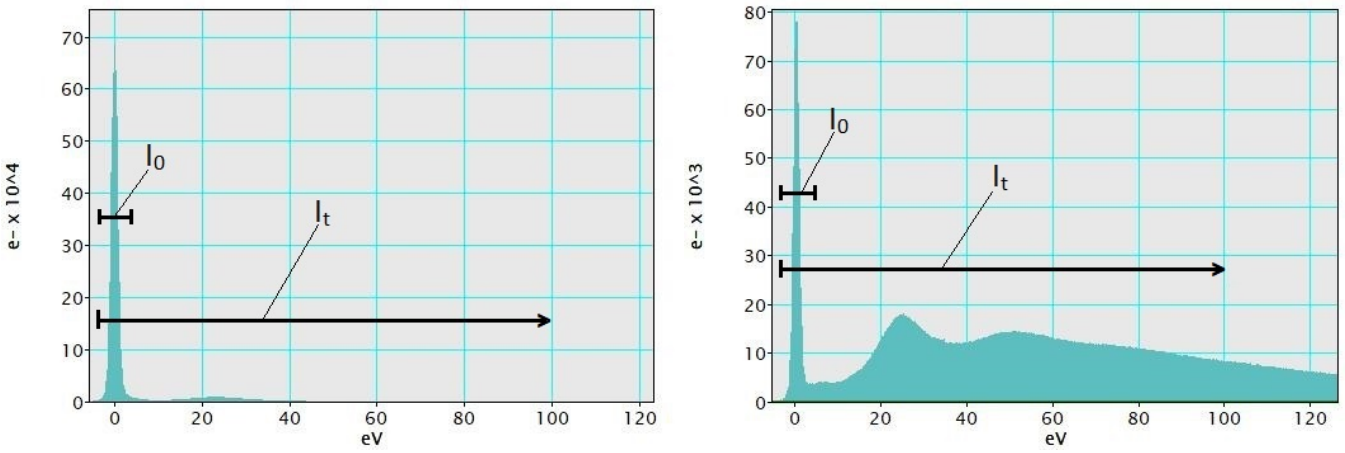

Figure 1.6: EEL spectra of two different measurements on a specimen with varying thicknesses. Left figure have a relative thickness of approx 0.2 t/λ while right figure has a relative thickness of approx 2.5 t/λ. Illustration of where the intensity regions for I_0 and I_t is located is also shown.

Plural scattering

When the specimen thickness increases, the probability for plural scattering also increases. This scattering occurs when electrons are inelastically scattered more than once and is unfavorable when investigating specimens with TEM-EELS. If the specimen has a thickness of over 100 nm the intensity of the edges will not increase anymore and the background will be higher than the intensity of the edge making it invisible.

Deconvolution methods

Deconvolution methods can be used to remove the effect of plural scattering, since plural scattering is a collection of independent events which leads to predictable statistics. Fourier-log deconvolution can be used if the EEL spectra contain a zero-loss peak otherwise Fourier-ratio deconvolution can be used. Deconvolution allows retrieving single scattering spectrum, and thereby reproducing the correct shape of ionization edges.

- The Fourier-log method removes the effect of plural scattering for the whole spectrum which has to contain a zero-loss peak. In this method, the spectrum is described as the sum of individual scattering components (zero-loss peak) and the single scattering spectrum, double-scattering spectrum, triple scattering spectrum and so forth. Each of these scattering spectrums are convoluted with a function that measure how much the spectrometer degrades the generated spectrum. This function is called the instrumental response function [52]. The Fourier transform of the whole spectrum is then given by equation 1.3 [43].

$$i^1(v) = z(v) ln \left[\frac{i(v)}{z(v)} \right] \tag{1.3}$$

Where:

$i^1(v)$ = is the single-scattering distribution
$i(v)$ = is the Fourier-transform of the recorded spectrum from the ZLP up to the core-loss of interest
$z(v)$ = is the reconvolution function

When extracting the single-scattering spectrum one would ideally do an inverse transformation of the single scattering transform i(v) but this will result in too much noise in the spectrum. There is however ways to avoid this and the easiest and simplest way is to approximate the zero-loss peak to a delta function [52]. Performing Fourier-log deconvolution is unfortunately not a flawless method and one have to take into account that artifacts can be introduced into the single-scattering spectrum. The overall result from this deconvolution is in most cases an increase in the ionization edge jump ratio. This will help detect small ionization edges from elements with low concentration or the presence of ionization edges from thick specimens [52]. An illustration of how this deconvolution looks like can be seen in figure 1.7.

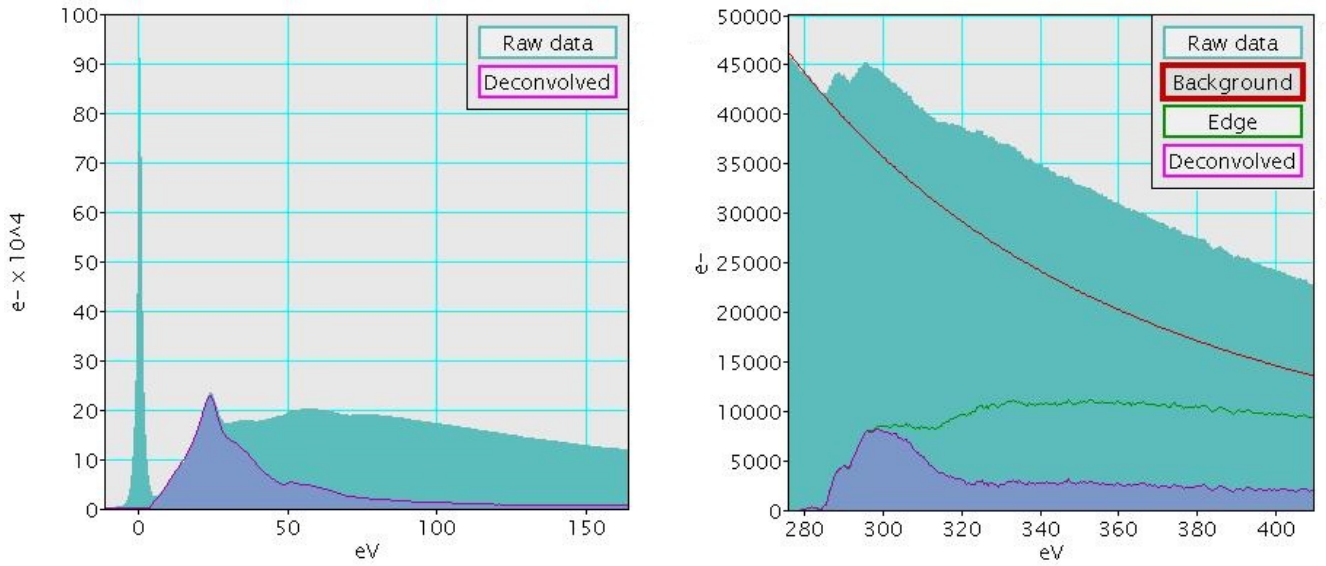

Figure 1.7: Fourier-log deconvolution of a specimen with a relative thickness of about 3.0 t/λ on the left and Fourier-ratio deconvolution of a specimen C K edge with a relative thickness of about 1.5 t/λ on the right.

· The Fourier-ratio method: This method approximates the experimental spectrum to an ideal single scattering spectrum which is convoluted with a low-loss spectrum. This yields the equation 1.4 [43].

$$i^1_{core}(v) = z(v) ln \left[\frac{i_{core}(v)}{i_{low}(v))} \right] \tag{1.4}$$

Where:

$i^1_{core}(v)$ = is the single-scattering distribution
$i_{core}(v)$ = is the Fourier-transform core-loss spectrum
$i_{low}(v)$ = is the Fourier-transform low-loss spectrum
$z(v)$ = is the reconvolution function

In this equation the instrument response is approximated by the low-loss spectrum rather than the ZLP. This method is well suited for EEL spectra that do not include a ZLP [20].

Shapes of EELS ionization edges

The shapes of ionization edges depend on the density of states and here is an overview of what basic shapes one can expect and also a brief introduction to why these shapes are formed (predicted by the free atom model). They are classified in four categories [14]:

- Hydrogenic edge with saw-tooth profile, rapid rise at the threshold followed by a graduate decay.
- Delayed maximum due to centrifugal-barrier effects. This gives a rounded edge with a maximum at least 10 eV above threshold energy.
- Sharp white-line peaks at the edge threshold, due to excitation to empty d-states (in transition metals) or f-states (in rare earths).
- Plasmon-like edge with the energy onset before the edge maximum. The energy given is that of the edge onset, not the intensity maximum.

Because of near-edge fine structures (ELNES) which depend on the chemical and crystallographic structure of a specimen, this classification can only serve as a rough guide. Elements such as copper exist in different valence states which give rise to dissimilar edge shapes. The edge onsets can vary by several electron volts, depending on the chemical environment of the excited atom.

Visual examples can be seen in figure 1.8.

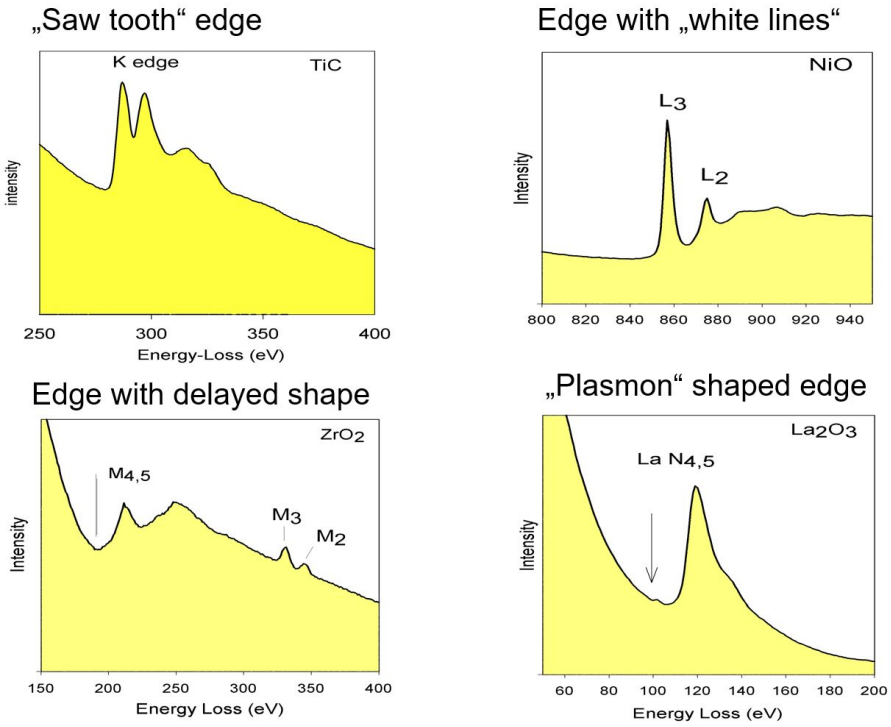

Figure 1.8: Examples of ionization edges

Elemental analysis

The raw data of the acquired EEL spectra contains the wanted edge intensities but unfortunately also background intensity. This background needs to be removed to further analyze the acquired data. For this purpose the background is modeled and then subtracted so only the edge intensities remain. The background model that is mainly used is the power law background model which can be described as equation 1.5 and a region before the onset of the edge is used to fit the background.

$$J(E) = AE^{-r} \tag{1.5}$$

Where A is a scaling constant and r is the slope exponent (usually 2 - 6).

It is possible to perform quantification on the acquired data, either doing absolute or relative quantification. For absolute quantification, equation 1.6 is used, which also takes into account plural scattering which needs to be considered. The acquired data has, for absolute quantification, to include a zero loss peak [20].

$$N \approx \frac{I_k(\beta, \Delta)}{I_{low}(\beta, \Delta)\sigma_k(\beta, \Delta)} \tag{1.6}$$

Where:

N = Number of atoms per unit area
$I_{low}(\beta, \Delta)$ = is the low-loss intensity integrated up to energy-loss window Δ
$\sigma_B(\beta, \Delta)$ = is the partial scattering cross-section integrated over a collection angle β and a energy-loss window Δ

If one investigates an energy-loss region that is not possible to include a zero loss peak, due to for example low dispersion, one can use the relative quantification instead. This quantification obtains an atomic-ratio of species A and B without the zero-loss integral and also partly corrects for artifacts including thickness and diffraction contrasts. The relative quantification can be written as in equation 1.7 [17][23].

$$\frac{N_A}{N_B} \approx \frac{I_A(\beta, \Delta)}{I_B(\beta, \Delta)} \frac{\sigma_B(\beta, \Delta)}{\sigma_B(\beta, \Delta)} \tag{1.7}$$

Where:

N_i = Number of atoms pr unit area
$I_i(\beta, \Delta)$ = is the core loss integrated up to energy-loss window Δ
$\sigma_i(\beta, \Delta)$ = is the partial scattering cross-section integrated over a collection angle β and a energy-loss window Δ

For quantification, ionization cross sections are necessary. They can be calculated theoretically by using one of the two different models [23].

- Hydrogenic model - This model was introduced by Egerton [18] where the partial cross-sections are calculated by assuming an atomic model that is based on the hydrogenic wave functions which are scaled to take into account the nuclear charge and then incorporate a single atomic-number dependent constant to account for screening. This model is good for ionization edges that exhibit a saw tooth profile where the K-shell ionization is a good example. There are however some limitations with this model, both for quantification of heavier elements ($Z > 30$) due to the use of higher order ionization that requires substantial correction near the ionization threshold. Another limitation is when Z is very low. Then the hydrogenic model tends to overestimate the cross section [19]. The benefit with this model is that it can also take into account white lines at the edge-onset.

- Hartree-Slater model - This model assumes that the elements are in atomic form and can be treated on the basis of a single electron inner-shell wave function undergoing a transition to the continuum. Here the theoretical cross-sections are derived from a Hartree-Slater central field model. This model can be applied to all inner shells as well as heavy elements. There is however some uncertainties with this model since neither solid state, excitronic effects nor transitions to unoccupied bound states are taken into account. This model is very versatile since in can be applied to all inner shells and also to heavy elements where the hydrogenic model is not as reliable any more [47].

It is also possible to determine the cross-section experimentally. One method is is the so called K-factor method. Here a thin film standard is used which has to contain one standard light elements (eg. called B) that gives a K edge in the experimentally obtained EEL spectra and the element (eg. called A) that is of interest. If the concentration of these elements are known. The cross-section ratio can be calculated using equation 1.8 [23].

$$\frac{\sigma_{_B}(\beta,\Delta)}{\sigma_A(\beta,\Delta)} = \frac{I_B(\beta,\Delta)}{I_A(\beta,\Delta)} \cdot \frac{N_A}{N_B} = k_{AB} \tag{1.8}$$

This method is preferably used on oxide compounds and have some advantages as for example that all elements and edges (up to O edges) can be quantified with good accuracy. The thickness determination is not necessary. Contamination layers (including thin amorphous layers) do not have an effect in the intensity ratios. Multiple scattering does not have a big impact on the result, because its effect on each edge cancels and lastly the K-factors can be viewed as effective "cross-sections" to take account of lens aberation effects. It turns out that cross-section ratios are not as dependent on the experimental conditions as absolute cross-sections. Therefore published K-factors make possible efficient EELS-quantification of data obtained under fairly similar experimental conditions in other laboratories. [23]

1.1.6 X-ray spectroscopy

X-rays are electromagnetic waves which are generated due to the electron-specimen interaction and it is the most important secondary signal generated in the specimen. From this signal it is possible to determine which elements are present in the investigated material. Two types of X-rays are produced [52].

- Characteristic X-rays
- Bremsstrahlung

In a TEM there is a high-energy beam that penetrates the specimen and therefore the electron pass though the outer conduction/valence bands and interacts with the core electrons. A consequence of these interactions is that there is a high possibility that atoms gets ionized and from there produces X-rays. Therefore it is possible to extract these signals from a TEM and can be used as a useful tool to get an overview of which elements that are present in the specimen. One big problem however with EDX is that the detection limit for light elements (up to boron) is low and therefore it is not possible to analyze these elements. A good schematic of how an EDX spectrum look like can be seen in figure 1.9.

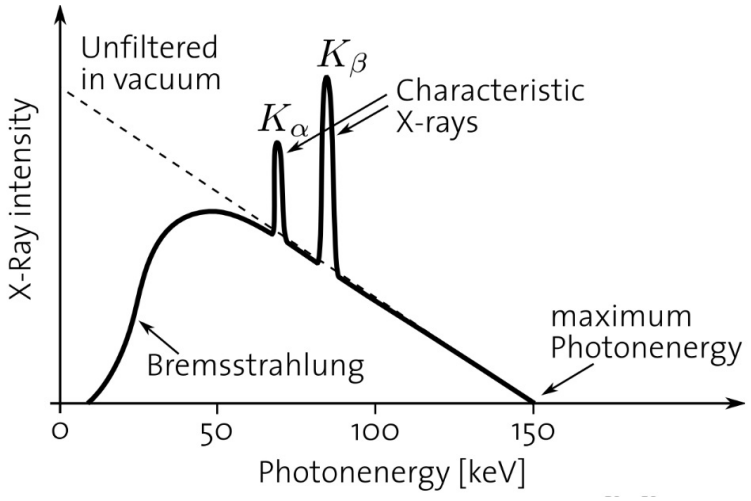

Figure 1.9: Schematics of an X-ray spectrum including Bremsstrahlung and the characteristic K lines [1].

Chapter 2

Description of the experiments and consequences for further studies

2.1 Experimental setup

2.1.1 FEI Tecnai F20

All the materials were investigated with the FEI Tecnai F20 operated at 200 keV. The FEI Technai F20 is a dedicated analytical electron microscope with a Schottky field emitter as a electron source and is equipped with a Wien-filter monochromator which can give an EELS energy resolution as good as 0.1 eV. This microscope is using an EDAX Sapphire Si(Li) detector and has a Gatan UltraScan CCD installed. The magnification range is between 25x - 2000kx [3].

2.1.2 Monochromator

In a normal TEM, the energy resolution of EELS is limited, but this can be overcome by using a monochromator. In the FEI Tecnai T20 a single Wien filter is used. A monochromator is an electron-optical system including energy-dispersive deflectors and an energy-selecting slit, and there are many types of deflectors and their combinations, which decide the inherent performance of the instrument. The single Wien filter works in a way that it seperates the electrons by their speed using the crossing magnetic and electrostatic fields and then one can put in a energy-selecting slit mechanically that chooses a portion of the dispersed electrons [29]. An illustration of how this filter works can be seen in figure 2.1.

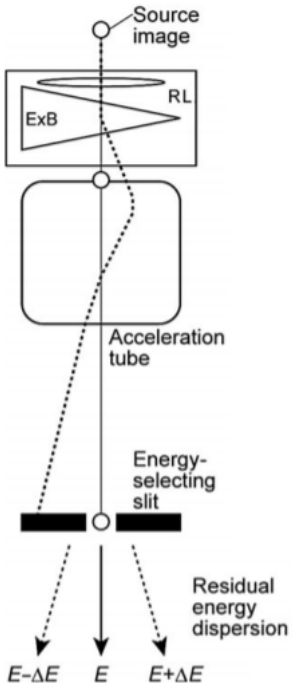

Figure 2.1: Illustration wien filter [29]

2.1.3 Gatan imaging filter

The Gatan imaging filter (GIF) is mounted below the column of a TEM and consists of two parts [7].

- Magnetic prism: Here electrons with different energies are dispersed due to a magnetic field. The electrons have different energies compared to the incident electron beam due to interaction with a specimen. This dispersion of the electron energies which is collected on the CCD camera are the basis of how the EELS are obtained.
- Optical column: Here an energy range can be selected by choosing a slit that is located at the dispersion plane. When in imaging mode, the electrons that have the energy within the energy range selected, can pass through the lenses of the optical system. This results in an energy-filtered image at the end of the GIF where you can find a slow-scan CCD camera for image recording.

An image of a GIF can be seen in figure 2.2.

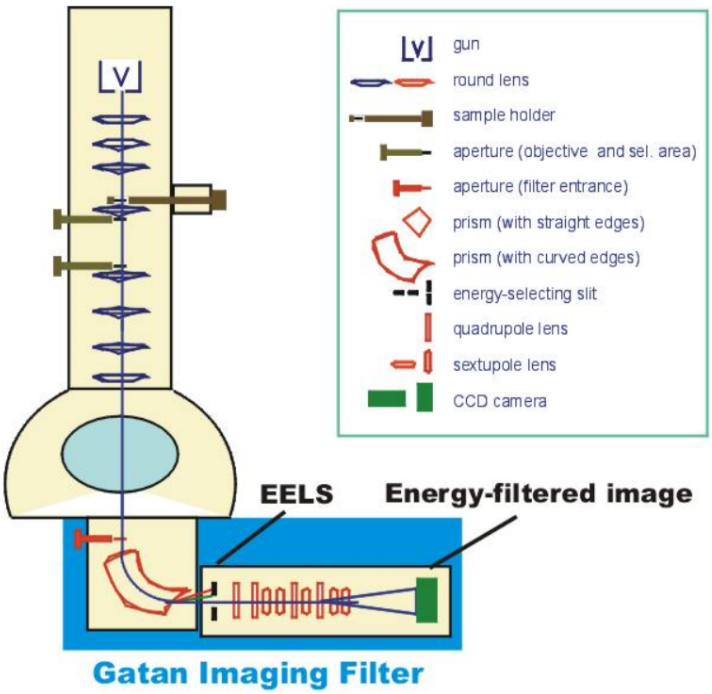

Figure 2.2: Illustration of a TEM with the Gatan imaging filter [7].

Since the magnetic prism is the most important part of these two regarding EELS it is worth going a little more in detail explaining the magnetic prism. A detailed overview of this prism can be seen in figure 2.3.

In this magnetic prism the electrons are deflected by about 90 degrees in a perpendicular uniform static magnetic field B. The size of the deflected angle the electrons experience is dependent of its velocity and the strength of the magnetic field (this is according to the Lorentz force law). Since the strength of the magnetic field should be the same it is only the electron energy that is different (i.e their energy) and therefore the electrons are dispersed in the magnetic field and an EEL spectrum is obtained. The detectors used in the GIF are usually either an array of photodiodes or a charge-coupling-device (also called CCD) which is combined with a suitable scintillator and a light-guide (for example fiber). There are however limitations for this type of EELS detection system and this is that one can and will experience spectrum drift in the energy dispersion direction. High voltage fluctuation and magnetic field creep are examples of why one can experience this drift [9].

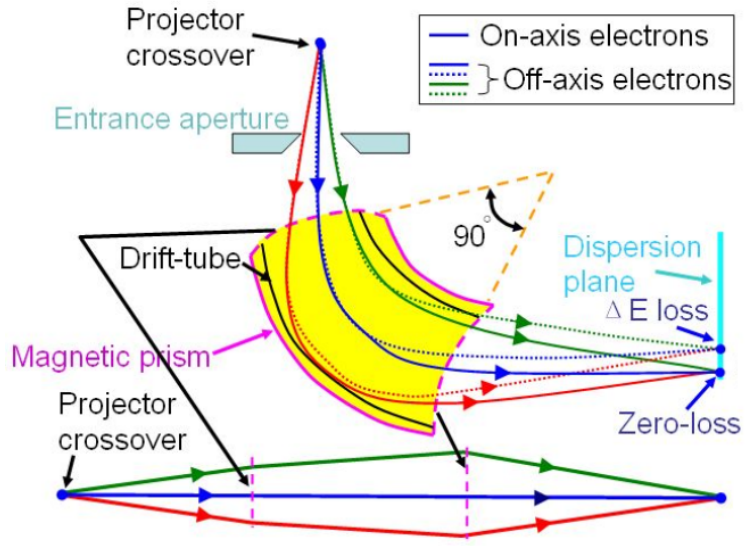

Figure 2.3: Illustration of the magnetic prism in the Gatan imaging filter [9].

2.1.4 EELS measurements

Since all the ionization edges of the materials that wanted to be investigated were lying around the same energy-loss range, it was decided that the same spectroscopy setup would be used for all the materials. If nothing else in mentioned, following parameters were used:

- Condenser 1 - Slit 1 which is wedge-shaped
- Condenser 2 - Set to 50 μm giving a convergence angle of 1.99 mrad
- Objective aperture - Set to 30 μm giving a collection angle of 8.7 mrad
- Monochromated accelerated mode with the Wien-filter, 800 V potential and exitation of 0.70
- All specimens were put into the cryoholder and cooled down with LN_2
- Dispersion was set to 0.1 eV/ch
- FWHM between 0.5 - 0.6 eV/ch

After the TEM was aligned, with correct focus and all parameters adjusted to get maximal resolution, the following steps taken to get the best EELS acquisition possible:

- First one had to find a specimen that seemed thin enough to do the EELS investigation
- When this specimen was found, the beam was moved slightly away from it and all the parameters were checked again to assure that nothing had changed
- The full width half maximum (FWHM) was also checked and tuned to get highest resolution possible.
- The beam was then moved back to specimen and EELS data was first acquired from the core-loss region to assure minimal beam damage
- After the core-loss spectrum was acquired, the ZLP/low-loss region was accuired which will be used for calibrating the core-loss data.

These steps was repeated on different places to compare data with each other.

2.1.5 Specimen holders

Mainly when doing measurements in the TEM, a cryoholder was used. A cryoholder is a special holder that can be filled with liquid nitrogen to cool down the specimen. This holder is a great tool to utilize especially to beam sensitive specimen (which will be proven later in this thesis) since a longer exposure of the electron beam is possible. The specific cryholder that was used is called Gatan CT3500 Cryotrans and it is a single tilt ultra high resolution nitrogen cooling holder with a cold shutter. It can be mentioned that when this holder first is filled up by liquid nitrogen, it is normal that drift occurs. Therefore one should wait around 30 minutes before doing measurement.

When the specimen did not need to be cooled down by LN_2, a double tilt FEI D537 specimen holder was used. This does not only tilt in β direction like the Gatan CT3500 does but also in α direction if needed.

2.1.6 TEM/EFTEM imaging

An unfiltered and a zero-loss filtered TEM image was taken in the region where the EELS measurements took place for each of the materials investigated to acquire a thickness map. This map can be used to get a rough idea what the relative thickness t/λ is and if the specimen is thin enough for EELS measurements. The TEM images also give an indication, although not prove, if the specimen has been modified in structure or not. The images were acquired after the EELS measurements to prevent unnecessary beam damage on the specimen and this resulted sometimes in visible beam damage on the images.

2.1.7 Specimen preparation

Various specimen preparation techniques were tried out, focused-ion beam milling (FIB), Ar-ion milling, ball milling or simply crushing the crystals. FIB is a good way to get very thin regions, but first of all it is very challenging to perform on these materials, very time consuming and also there is a chance that Ga ions can cause specimen damage (amorphization, temperature increase). Ball milling gave small particles as expected although it was observed that this method destroyed the crystallinity of the materials and therefore ball milling was not used any more.

Simply crushing the crystals were proven to be a very quick and successful technique, even though some attempts were necessary to produce specimens that had thin enough particles. The procedure was as follows:

- A small piece of the minerals was extracted and cleaned in ethanol.
- The pieces were then put into the mortar and crushed with a pestle for a short period of time till the sample had a powder-like consistence.
- This powder was then added to either ethanol or distilled water in a beaker.
- Using a ultrasonic bath, this was mixed together.
- The solution was then set to rest for a short period of time so that the remains of the ethanol evaporated, before a drop was extracted with a pipette and drop-cast on a copper grid coated with a holey carbon film. After around 30 minutes it had dried and the specimen was ready for investigation.

2.2 Control of beam damage

2.2.1 Beam Current

The beam current had to be measured and this can be done in two ways. One can either, according to the TF20 manual, look at the exposure time, which is in this case the value for the fluorescence screen suggested by the TF20, and the emulsion setting value (this value needs to be checked for the specific microscope) and then use equation 2.1.

$$Beam\ current(in\ nanoAmps) = 2.15\ x\ emulsion\ setting/exposure\ time \tag{2.1}$$

Another possibility is to take an image where the whole beam is present on the image (see fig.2.4). Here it is important that the CCD is calibrated and then use the program Digital Micrograph to measure the beam current by knowing total counts on the image and exposure time. Calculating the beam current from equation 2.1 gave a result of 0.41 nA while the measurement on the CCD gave a result of 0.32 nA.

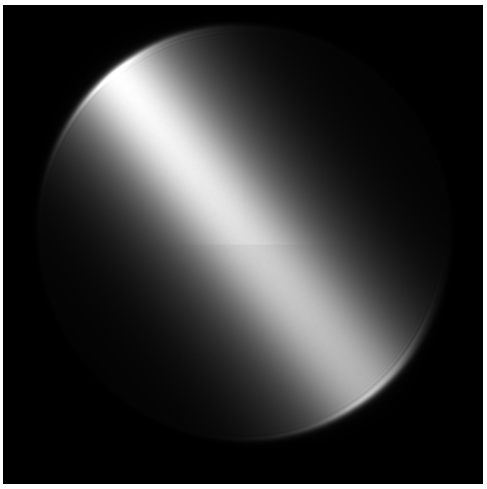

Figure 2.4: GIF of the beam to measure current using Digital Micrograph. The value of the current was measured to be 0.32 nA. If looked closely on the image one can see there is a difference in intensity in the upper half of the image compared to lower part. This is due to a problem with the CCD.

The results are quite different but this might be because there was, at the time of the measurement, a problem with the CCD that gave different intensities on upper half of the image compared to the lower part. The screen readout is also not completely reliable and for these reasons the measured current is questionable.

2.2.2 Beam damage effect on sample

In this part of the experiment, the effects of beam damage in TEM images and diffraction patterns were investigated. In figure 2.5 one can see in (a) an unfiltered TEM image with electron diffraction (b) taken in the same area, before the specimen was experiencing beam damage. The electron diffraction pattern indicate that the specimen clearly is crystalline.

After the specimen has been exposed to the electron beam over a longer time, the unfiltered TEM image (c) indicate that there has been structural modifications to the specimen and mass loss. The electron diffraction (d) was taken where this beam damage had occured and shows a combination of amorphous and crystalline regions.

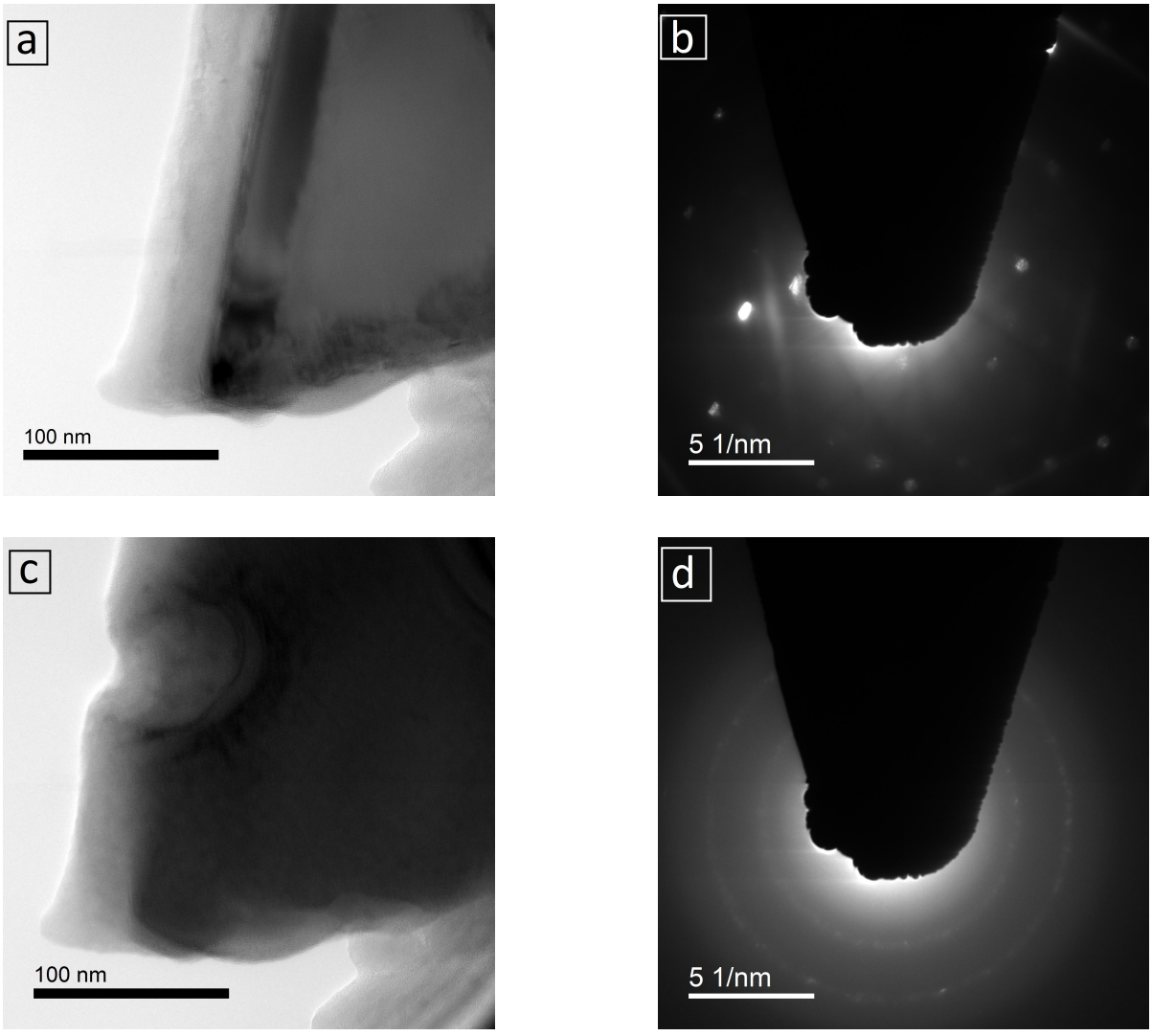

Figure 2.5: (a) Overview of a spodumene specimen without observed beam damage, (b) electron diffraction of (a) that clearly shows crystallinity, (c) Overview of a spodumene specimen with observed beam damage and (d) electron diffraction of (c) that shows a combination of amorphous and crystalline regions.

EELS were also performed in these areas to see the impact of beam damage had on chemical composition. Since the Li K edge acquired here have some similarities to the LiF one can assume that the main reason for the beam damage is the same. For fluorides and lithium compounds like e.g LiF, the damage is due to ionization process whose cross-section decrease with increase of acceleration voltage. From this one can conclude that a higher voltage is prefered [16]. This ionization unfortunately cannot be suppressed but only reduced by reducing total electron dose and also by cooling, e.g liquid nitrogen. The cooling slows down the diffusion process although this beneficial effect on beam damage on radiolysis is still not really understood [16]. The benefit of cooling the specimen with liquid nitrogen was tested out by comparing the changes over time with and without specimen cooling. Following was done to preform the EELS:

- Thin regions were searched for and when found the beam was quickly removed from this region.
- All the calibrations were done right next to the area needed to be investigated.
- When everything was set, the electron beam was moved to the desired area and data were acquired. Every 10 seconds (20 seconds with cryoholder) the acquisition was restarted and new data collected. This was done until there was no longer a major change in the results.

The EEL spectra for the uncooled specimen (298 K) can be seen in figure 2.6 and one can see that the Li K edge already starts to decrease after only 30 seconds and then completely disappear after 90 seconds. When cooling the specimen down with liquid nitrogen (77 K) using a cryo holder, the outcome is different and the result can be seen in figure 2.7. Here the Li K edge intensity only starts to decrease visibily after around 240 seconds which means eight times longer exposure times are possible with a cooled specimen. The edge is completely gone after around 420 seconds. From this observation it is quite clear that a cooled specimen is prefered when doing investigation to ensure that the specimen is as intact as possible.

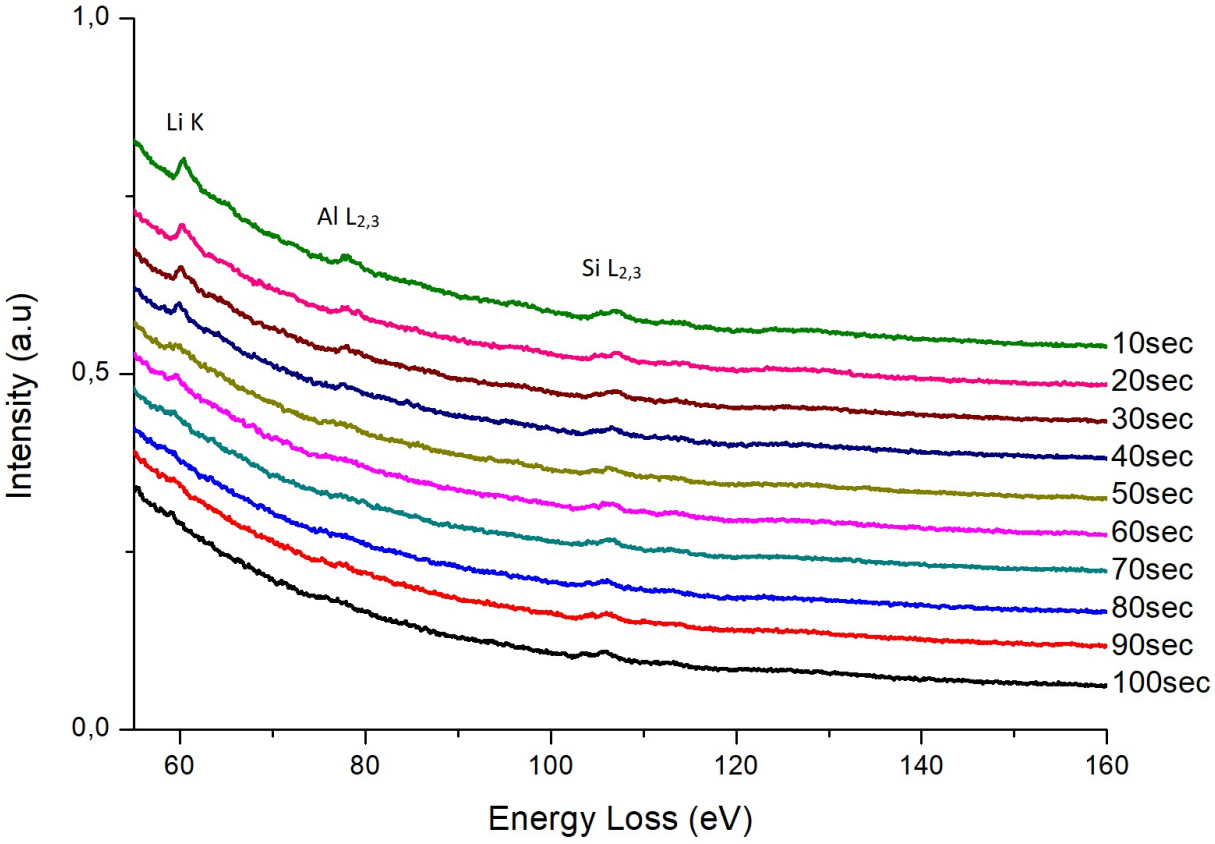

Figure 2.6: Overview of beam damage on spodumene over time in room temperature, 298 K .

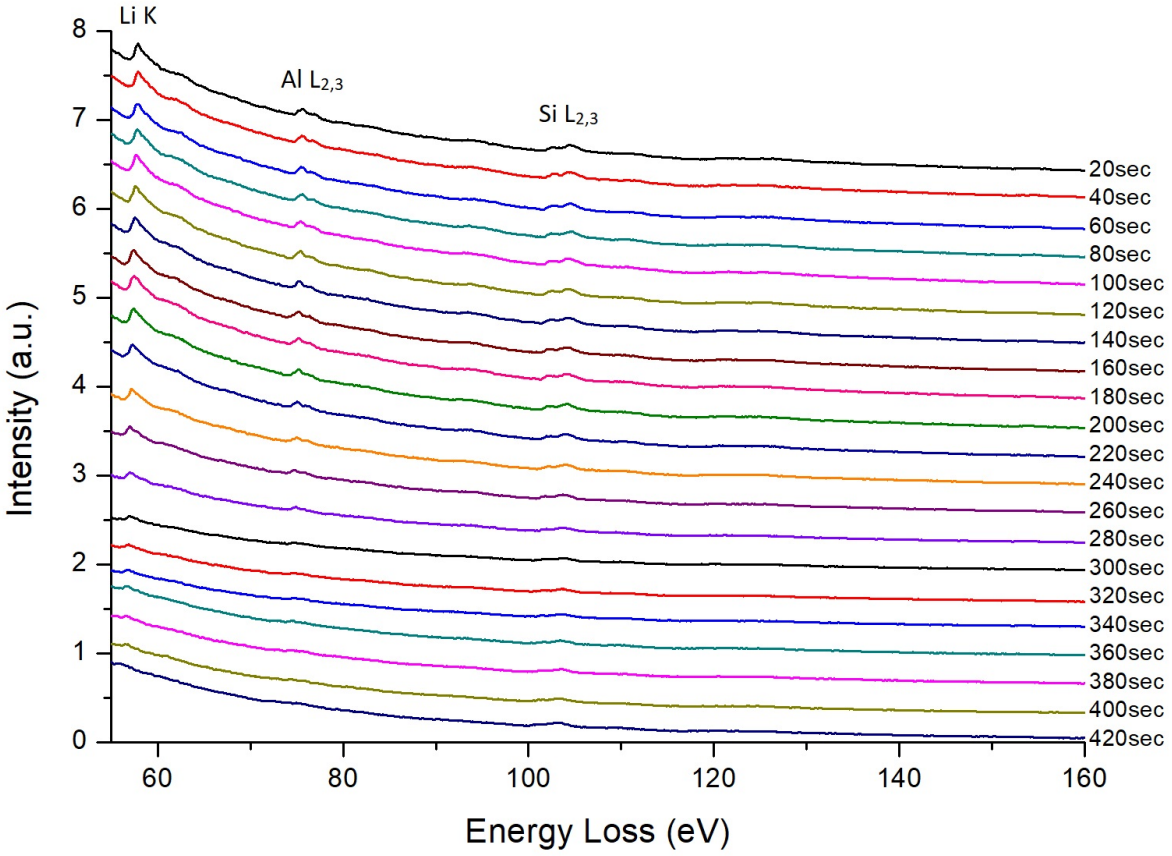

Figure 2.7: Overview of beam damage on spodumene over time using a cryoholder cooling the specimen down to 77 K.

Chapter 3

Results

3.1 Spodumene as test sample for quantification

3.1.1 General information about spodumene

Spodumene (Greek for "burnt to ashes" referring to the ashy color of early specimens) was first described in the 1800 in Sweden but later discovered by a Brazilian naturalist named Jose Bonifacio de Andrada e Silva and has a chemical composition of $LiAlSi_2O_6$. Spodumene is mainly an important source for high-purity lithium which then can be used in ceramics, Li-ion batteries and medicine to mention some applications. The lithium can be extracted by the use of acid. Just from this mineral, over 80.000 tons of lithium were produced every year where the Greenbushes Mine of Western Australia was the main contributors to this production [12]. Throughout most of the 20^{th} century, this mineral was the main source of lithium but after the discovery of lithium brines in South America this is no longer the case anymore. It is although still used as a source for high-purity lithium when the demand of lithium is higher than what these brines can produce [4].

The crystal system for α-spodumene is monoclinic but changes to a tetragonal crystal system at higher temperatures above 875K. Since α-spodumene is the stable phase, this will be explained more detailed: α-spodumene belongs to a crystal family of clinopyroxenes which has a general composition of AMX_2O_6 where in this case the crystal structure consists of SiO_2 tetrahedra chains that go along the c axis and they are interconnected by AlO_6 octahedra chains and irregularly shaped polyhedra of six-fold coordinated lithium ions [28]. This crystal structure is shown in figure 3.1 together with an image of the spodumene mineral used for investigation in this thesis.

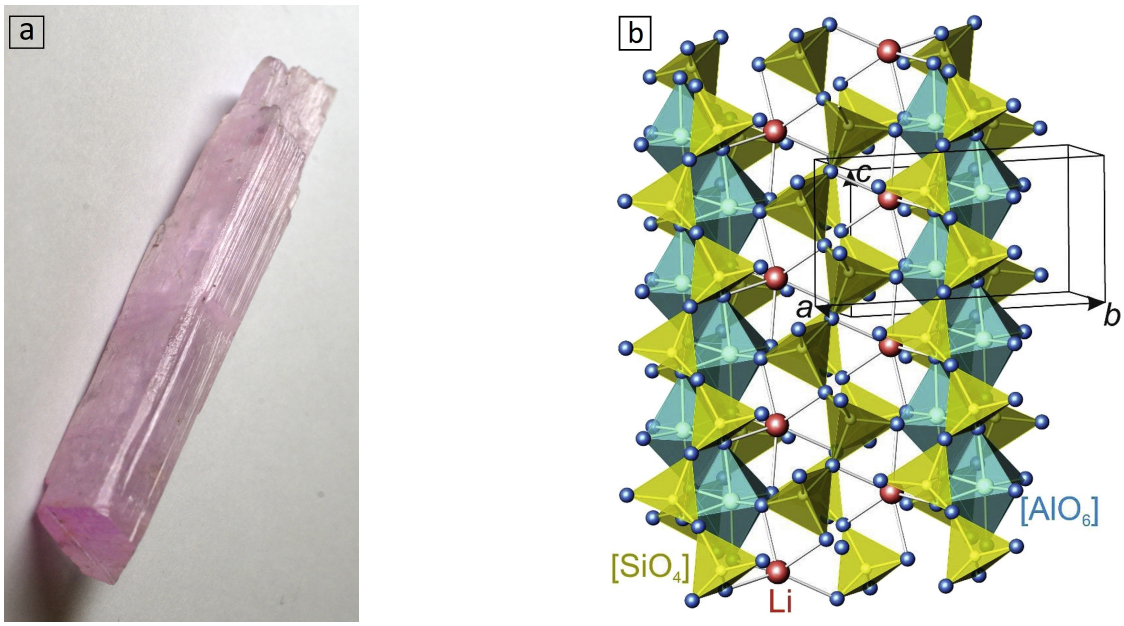

Figure 3.1: (a) Investigated spodumene sample from Pakistan (by M. Wallner) (b) crystal structure of spodumene [28].

3.1.2 TEM/EFTEM investegation

The unfiltered and the zero-loss filtered images with the resulting thickness map can be seen in figure 3.2. From this thickness map, the relative thickness t/λ was examined in the marked area where the EELS measurements took place and the average relative thickness was 0.5 t/λ. There are also no obvious structural modifications on the specimen observed.

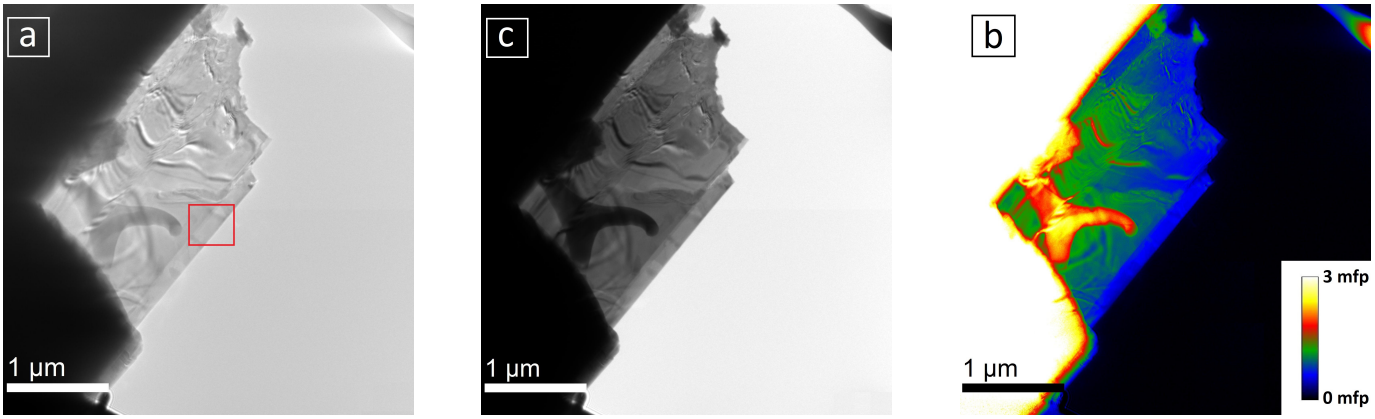

Figure 3.2: (a) Unfiltered TEM image, (b) zero-loss filtered TEM image and (c) resulting relative thickness map.

3.1.3 EDX spectroscopy

The result of the EDX data acquired for the spodumene specimen can be seen in figure 3.3. The EDX shows the Al Kα peak 1.5 keV, Si Kα peak at 1.75 keV, O Kα peak at 0.53 KeV and C Kα peak at 0.28 KeV. Lithium is not possible to detect as explained previously. The carbon is most likely from the carbon grid that is used. There is also possible that the carbon is due to a contamination on the specimen but when looking at the EEL spectrum from the same area, carbon was not detected. Other materials visible in the spectrum (Cu, Fe and Co) are due to the specimen holder and the material in the TEM column and can be disregarded.

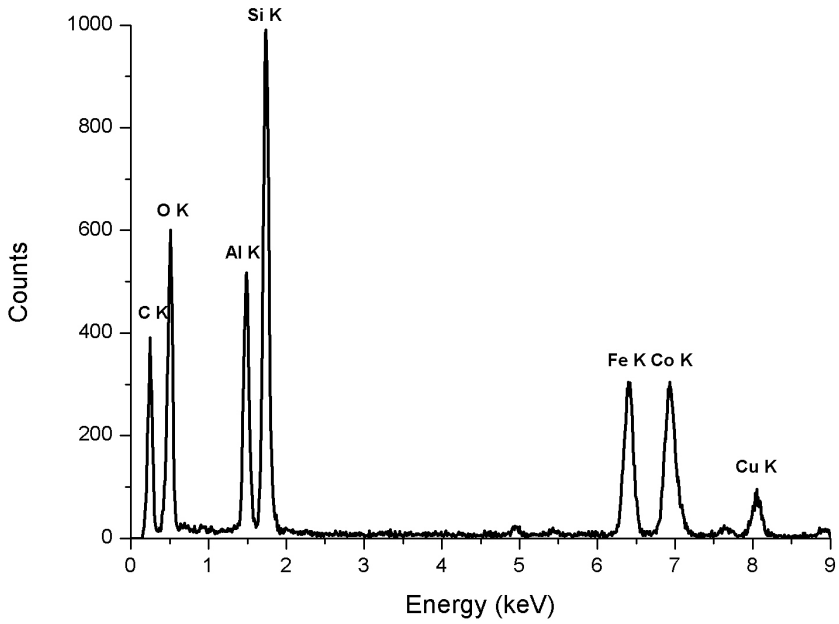

Figure 3.3: EDX spectrum of spodumene (including Fe, Co and Cu contamination signals from the TF20 and sample holder) recorded from the specimen region shown in figure 3.2.

3.1.4 Monochromated EEL spectroscopy

A raw monochromated EEL spectrum with background and spectrum with background substracted of spodumene from the specimen region is shown in figure 3.2 and the spectra showing each edge in detail can be seen in figures 3.5 - 3.8 including the K edge of oxygen. At 60 eV one can see the strong K "saw tooth" edge of lithium, followed by the $L_{2,3}$ edge of aluminium at 77.5 eV, $L_{2,3}$ edge of silicon at 105 eV and the K edge of oxygen at 532 eV.

This EEL spectrum resembles all the features of the EEL spectrum measured by [25] by using a TEM-EELS system with an energy-resolution of around 1 eV. Our spodumene spectrum is the first one, which has been recorded with high energy resolution well below 0.6 eV and consequently we are able to reveal more detailed near edge fine structure features (ELNES). The K edge of lithium looks quite different to those ones found in Li_2O, Li_2CO_3 and LiF [39] which is mainly caused by the different chemical coordination of the Li-ion. It is also possible to see the spin-orbit splitting at the $L_{2,3}$ ionization edges as previously revealed by investigating α-Al_2O_3 and α-SiO_2 by EELS (unpublished data by Katharina Riegler, 2009) and by X-ray absorption spectroscopy [40].

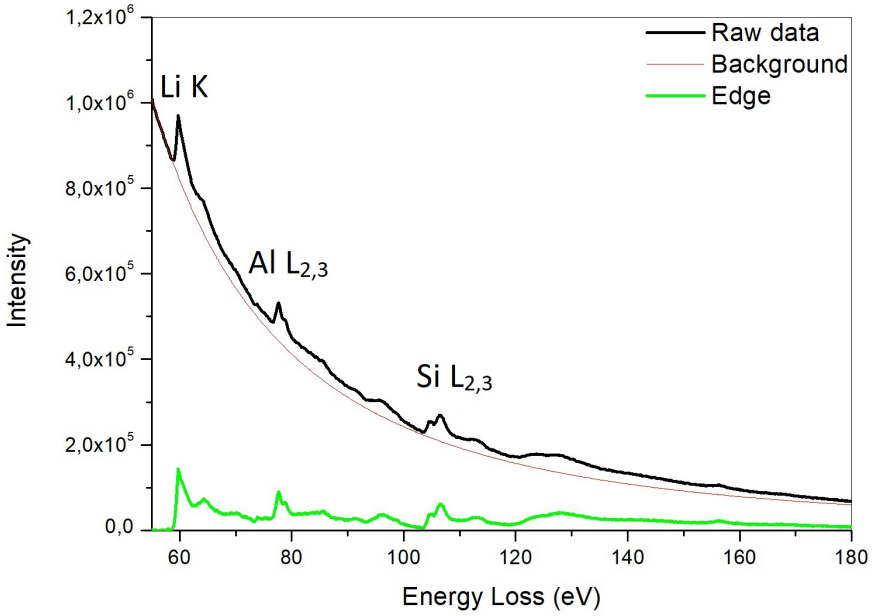

Figure 3.4: Raw monochromated EEL spectrum with background and spectrum with background substracted of spodumene from the specimen region shown in figure 3.2.

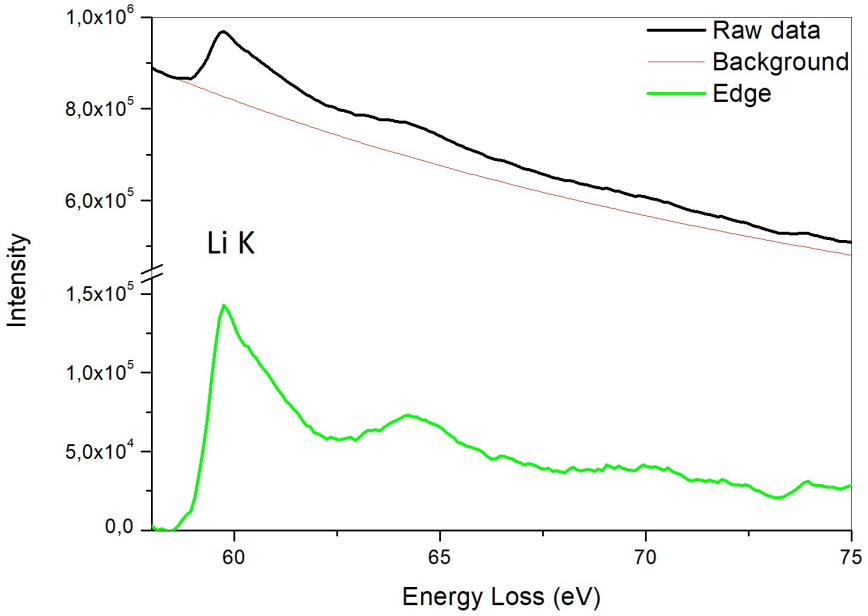

Figure 3.5: K edge of lithium with and without background taken from figure 3.4.

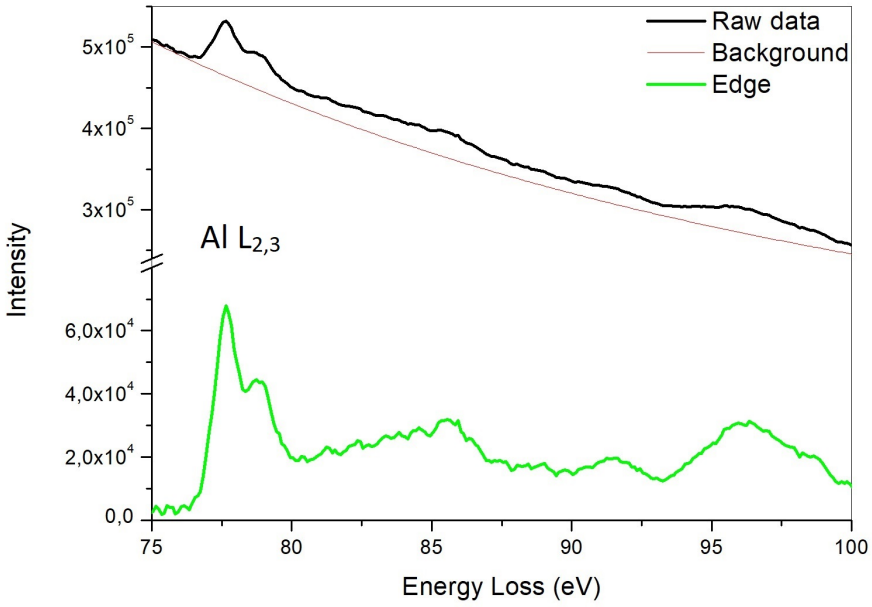

Figure 3.6: $L_{2,3}$ edges of aluminium with and without background taken from figure 3.4.

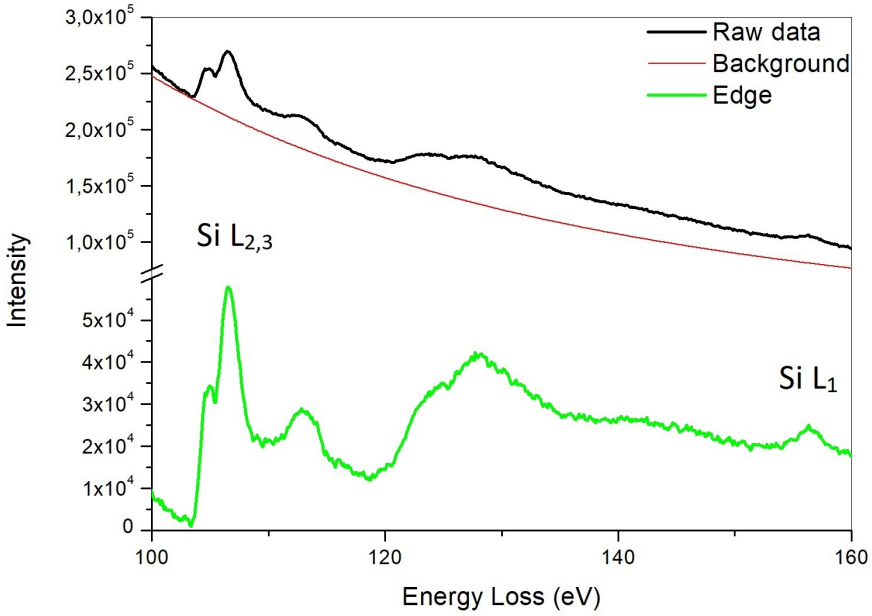

Figure 3.7: $L_{2,3}$ and L_1 edges of silicon with and without background taken from figure 3.4.

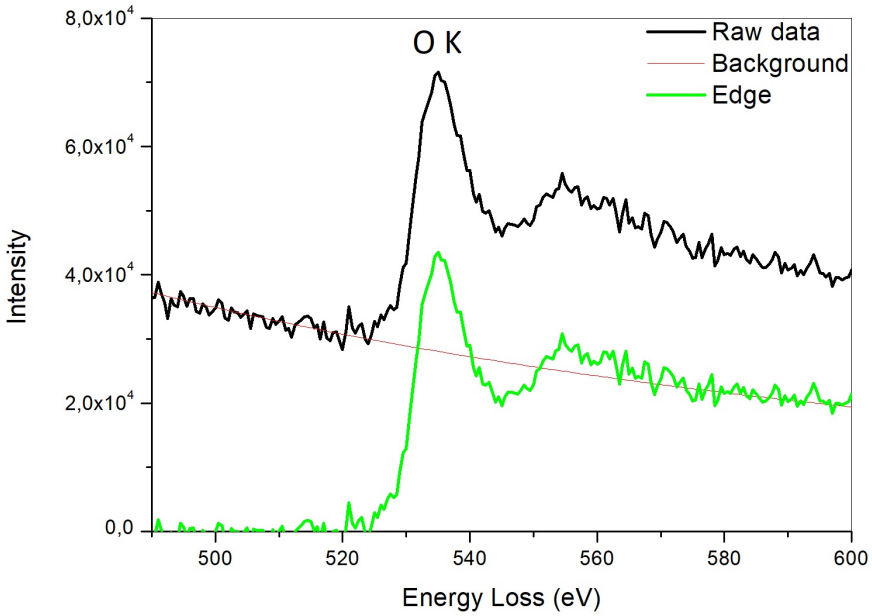

Figure 3.8: K edge of oxygen with and without background with following changes in the experimental conditions:: 0.5 eV/ch dispersion, non-monochromated with $\beta = 14.3$ mrad and $\alpha = 6.06$ mrad in room temperature.

3.1.5 Quantitative analysis

Three spodumene specimens with different experimental conditions were quantified using corresponding EEL spectra and then compared using the program Digital Micrograph GMS version 2.32.880.0 with variations of ionization cross-section models were tested out on the lithium K edge. In table 3.1 one can see the results of the three different quantifications performed on the spodumene. An integration over an interval of 16.7 eV for the Li K edge ionization cross-section were also performed for these three specimens and the integrated values (in barn) can be found in table 3.2.

Table 3.1: Results of EELS quantifications of spodumene. Atomic ratios have been determined using calculated cross-sections with both hydrogenic model and Hartree-Slater model for lithium K edge and only Hartree-Model on other elements. Experimental conditions: E_0 = 200 keV, β = 8.7 mrad and α = 1.99 mrad

Spodumene	At. ratio	Nom.	Hydro.model Li(K edge)	Hartree-Slater Li(K edge)
Room temp (298K)	Li/Si	0.5	0.40 ± 0.056	0.68 ± 0.097
	Al/Si	0.5	0.68 ± 0.097	0.65 ± 0.092
	Li/Al	1.0	0.58 ± 0.056	0.95 ± 0.097
Cooled w/o ghost peak	Li/Si	0.5	0.50 ± 0.071	0.81 ± 0.114
	Al/Si	0.5	0.39 ± 0.055	0.39 ± 0.055
	Li/Al	1.0	1.30 ± 0.071	2.09 ± 0.114
Cooled w/ ghost peak	Li/Si	0.5	0.54 ± 0.076	0.86 ± 0.122
	Al/Si	0.5	0.49 ± 0.069	0.49 ± 0.069
	Li/Al	1.0	1.08 ± 0.076	1.76 ± 0.122

Table 3.2: Comparing integrated values in barn between hydrogenic and Hartree-Slater model for Li K edge cross section within an energy window of 16.7 eV (57.1 eV - 73.8 eV) for the three different measurements shown in table 3.1. Experimental condition: E_0 = 200 keV, β = 8.7 mrad and α = 1.99 mrad

Sample	Hydrogenic model (barn)	Hartree-Slater model (barn)	Difference
Room temp (298 K)	48474	29565	39%
Cooled w/o ghost peak	52191	32459	38%
Cooled w/ ghost peak	52544	32659	38%

The ionization cross-section models (GMS 3.20.1314.0) for the Li K edge, Be K edge and O K edges were also extracted and compared. The graphs from these models can be seen in figures 3.9 - 3.11. Integrated values (in barn) for the first 30 eV in these graphs can be seen in table 3.3.

Table 3.3: Comparing integrated values in barn between Hydrogenic and Hartree-Slater model for Li K edge, Be K edge and O K edge cross section within an energy window of 30 eV using following experimental conditions: E_0 = 200 keV, β = 8.7 mrad and α = 1.99 mrad

Element	Hydrogenic model (barn)	Hartree-Slater model (barn)	Difference
Li K edge (55 eV - 85 eV)	757433	515787	32%
Be K edge (111 eV - 141 eV)	209970	159731	24%
O K edge (532 eV - 562 eV)	8526.5	7711.25	10%

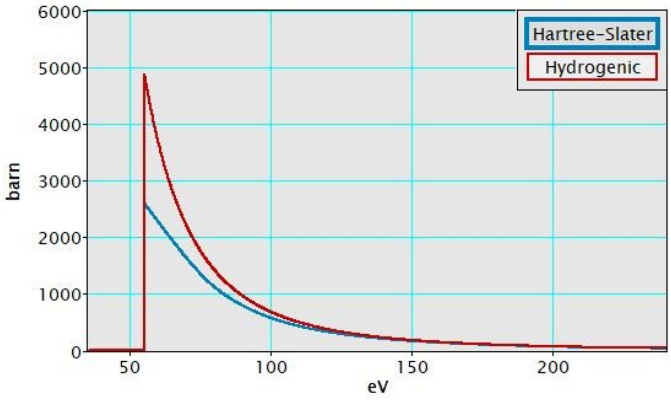

Figure 3.9: Comparison between hydrogenic and Hartree-Slater model for lithium K edge using GMS (3.20.1314.0).

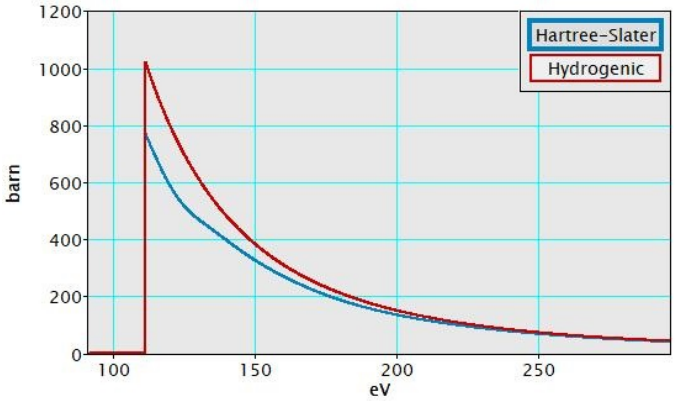

Figure 3.10: Comparison between hydrogenic and Hartree-Slater model for beryllium K edge using GMS (3.20.1314.0).

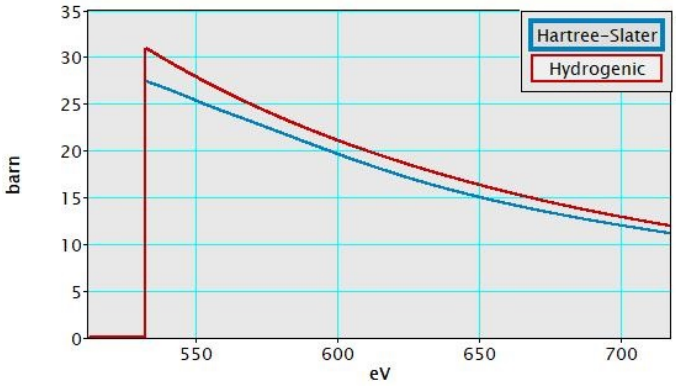

Figure 3.11: Comparison between hydrogenic and Hartree-Slater model for oxygen K edge using GMS (3.20.1314.0).

3.2 Triphylite as test sample for phosphates

3.2.1 General information about triphylite

Triphylite (which means "family of three" in Greek, referring to iron, manganese and lithium) was discovered in 1834 by a German mineralogist by the name Johann Nepomuh von Fuchs. Triphylite can both describe a mineral series as well as an individual mineral within the series. Triphylite is the iron-rich end member of the triphylite series with a chemical composition of $Li(Fe^{2+},Mn^{2+})PO_4$ with varying range of manganese and lithophilite is the manganese-rich end member. These minerals are not the same as $LiFePO_4$ nor $LiMnPO_4$, since these are artificial ceramics [41], although the mineral is isostructural with them [22].

An image of the mineral that was investigated can be seen in figure 3.12 together with the crystal structure, which has an olivine structure, in other words, an orthorhombic system with Pnma space groups. The oxygen has a distorted hexagonal-close-packed framework which contains lithium and iron (or manganese) located in half of the octahedral sites. The phosphorus ions are located in 1/8 of the tetrahedral sites. The LiO_6 octahedra form edge-sharing chains along the b-axis and the FeO_6/MnO_6 octahedra are corner-shared and are linked together in bc-plane. The PO_4 tetrahedral group share a common edge with one of the FeO_6/MnO_6 octahedra and two of the edges with LiO_6 octahedra [54].

Triphylite can be used as a source for lithium and can for example be found in Hagendorf in Bavaria. Here over 1.800 tons of triphylite was melted so that lithium could be extracted out [6].

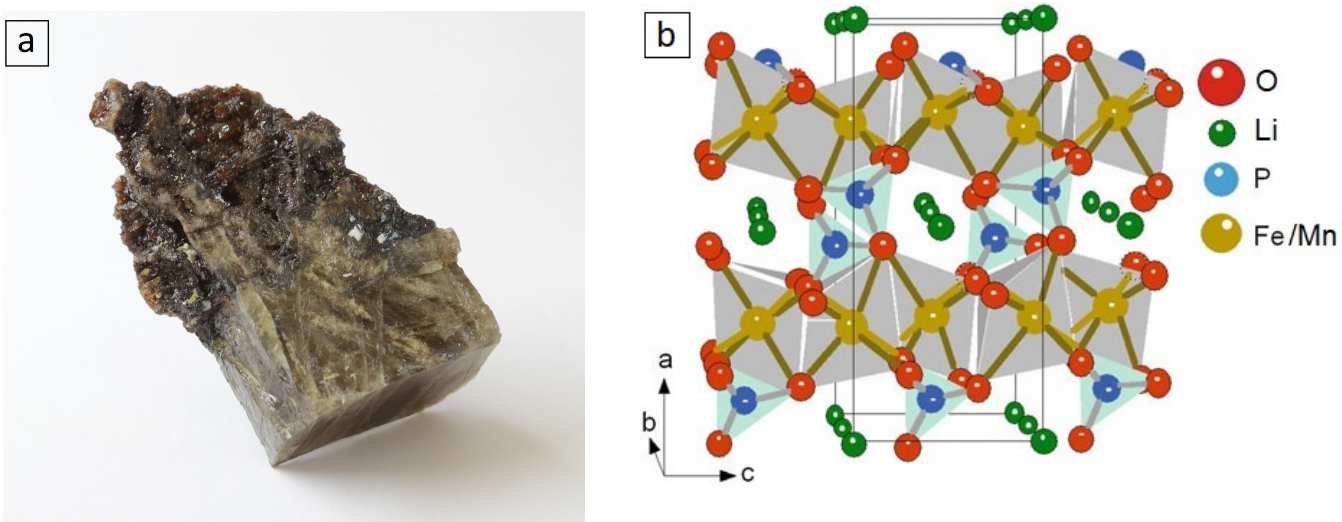

Figure 3.12: (a) Investigated triphylite sample (by M. Wallner) (b) crystal structure of triphylite [54].

3.2.2 TEM/EFTEM investigation

The unfiltered and zero-loss filtered images with the resulting thickness map can be seen in figure 3.13. From this thickness map, the relative thickness t/λ was examined in the marked area where the EELS measurements took place and the average relative thickness was 0.3 t/λ. Here, due to beam damage, the specimen structure was modified during the acquisition of the TEM images. The t/λ is therefore a bit misleading and the relative thickness of 0.5 t/λ from the EELS measurements are more reliable.

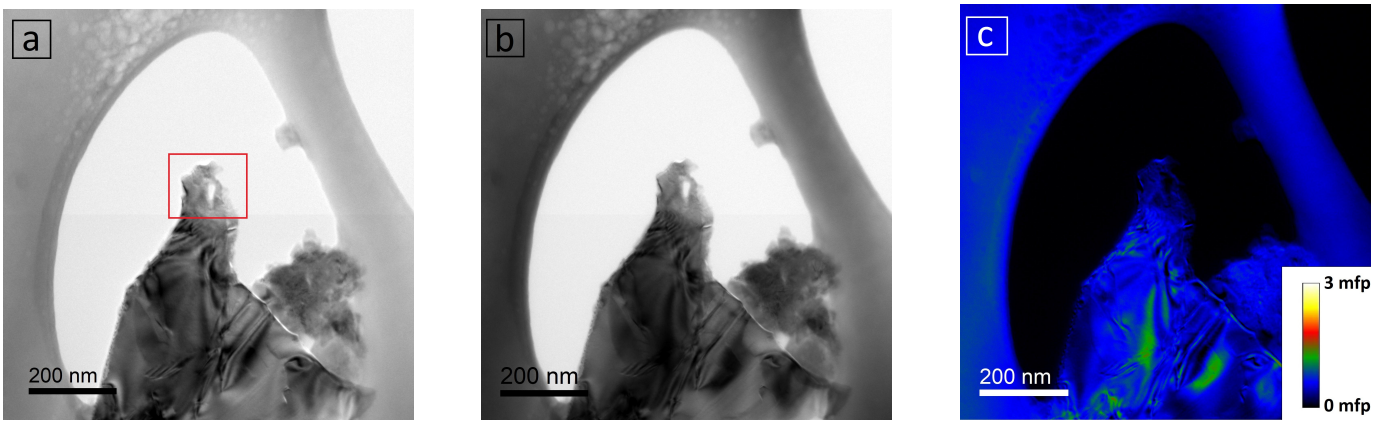

Figure 3.13: (a) Unfiltered TEM image, (b) zero-loss filtered TEM image and (c) resulting relative thickness map.

3.2.3 EDX spectroscopy

EDX was performed using a SEM to both confirm that all the material except the lithium was present but also to see if there might be some obvious contamination on the sample. Another reason why the EDX was performed by a SEM and not the TEM is to avoid readings of Co, Fe and Cu one normally would expect from TEM EDX. The result can be seen in figure 3.14. The results are showing clearly the presence of C Kα at 0.28 keV, O Kα at 0.5 keV, P Kα at 2 keV, Mn Kα at 5.9 keV and Fe Kα at 6.4 keV. Again as for spodumene the C Kα can either be from grid or contamination. From the EELS results presented in this report there was no observation of carbon and is therefore assumed that this carbon is from the grid.

The concentration of the elements (except Li) including K-ratio were also calculated and are shown in table 3.4 and the element concentration and K-ratio of Fe/Mn was looked more into detail and can be seen in table 3.5. This shows that the investigated triphylite have a ratio close to 50/50 of Fe and Mn.

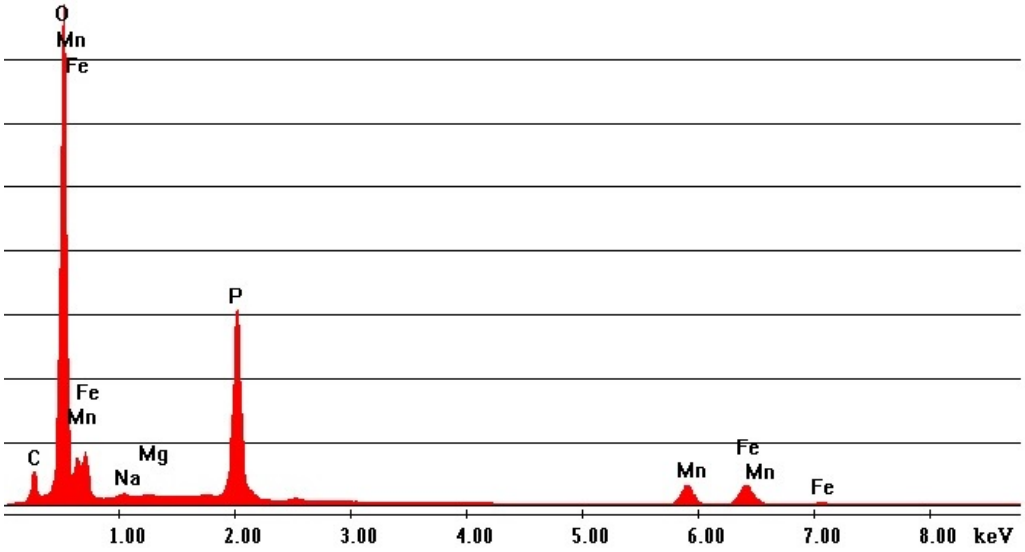

Figure 3.14: EDX spectrum of triphylite acquired from a SEM (by S.Šimić).

Table 3.4: Element concentrations and K-ratio of triphylite using SEM EDX.

Element	Wt %	At %	K-ratio
O K	46.20	69.85	0.3101
P K	19.36	15.12	0.1637
Mn K	16.16	7.12	0.1352
Fe K	18.27	7.91	0.1549

Table 3.5: Element concentrations and K-ratio of Fe and Mn in triphylite using SEM EDX.

Element	Wt %	At %	K-ratio
Mn K	47.03	47.44	0.4659
Fe K	52.97	52.56	0.5339

3.2.4 Monochromated EEL spectroscopy

The EEL spectrum of triphylite (fig.3.15) has been recorded from the specimen region shown in figure 3.13. Detailed spectra of the edges can be seen in figures 3.16 - 3.18. The strong $M_{2,3}$ edge of manganese is observed at 49 eV followed by the $M_{2,3}$ edge of iron consisting of a pre-peak at 54 eV and the main peak at 57.5 eV. The K edge of lithium at 60 eV is barely visible and exhibits the typical "saw-tooth" edge shape which is quite similar to the Li K edge in spodumene. The $L_{2,3}$ edge of phosphorus starts at 135 eV showing a near-edge fine structure (ELNES) which is typical for the phosphate anion (PO_4^{3-})[24].

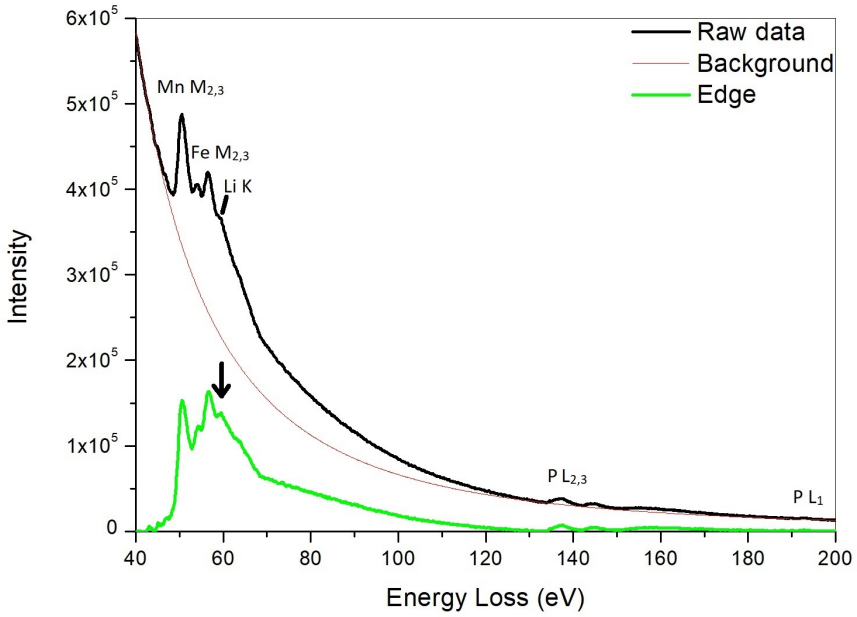

Figure 3.15: Raw monochromated EEL spectrum with background and spectrum with background substracted of triphylite from the specimen region shown in figure 3.13.

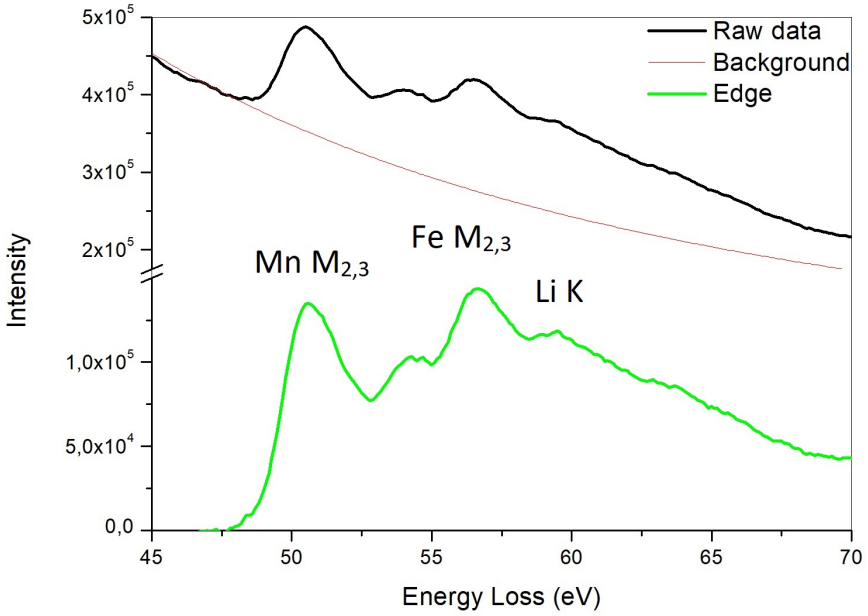

Figure 3.16: $M_{2,3}$ edges of manganese and iron including K edge of lithium with and without background taken from figure 3.15.

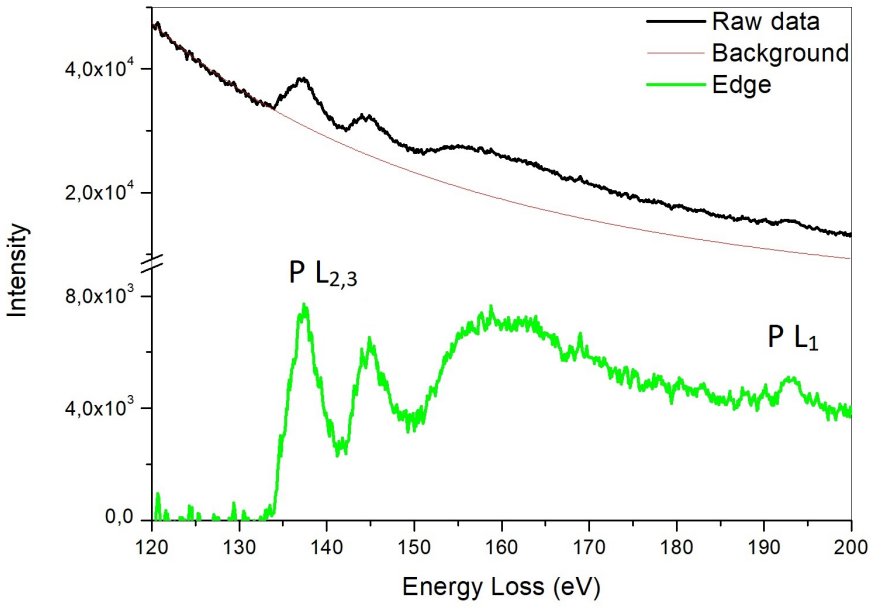

Figure 3.17: $L_{2,3}$ and L_1 edges of phosphorus with and without background taken from figure 3.15.

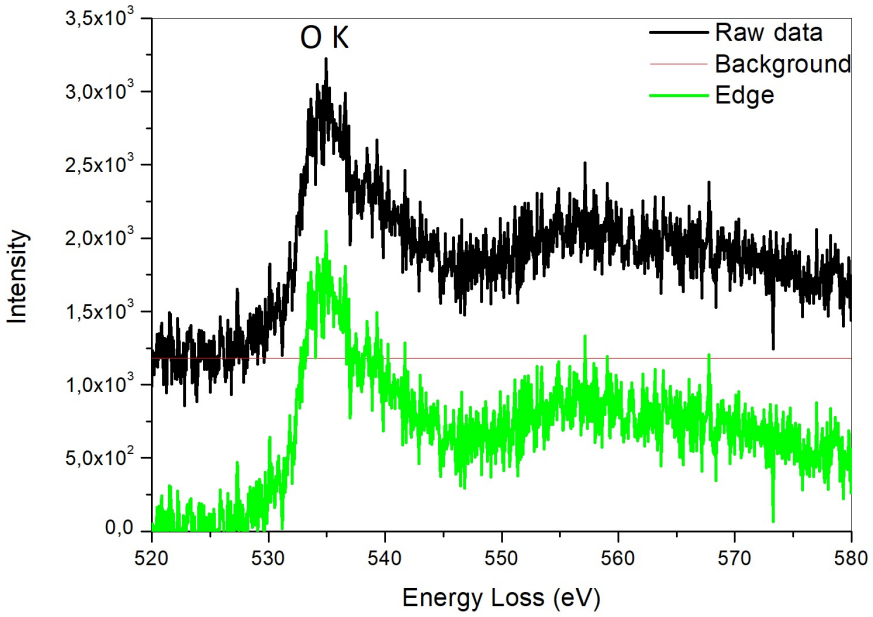

Figure 3.18: O K edge with and without background with following changes in the experimental conditions:: 0.05 eV/ch dispersion and non-monochromated.

3.3 Iron oxide

To confirm that there are two Fe $M_{2,3}$ edges, one pre-edge and one main edge at 53 - 58 eV, where the position of the pre-edge is determined by the oxidation state of the iron, an Fe_2O_3 specimen was investigated to confirm Fe^{3+}. The zero-loss TEM image of the investigated specimen at room temperature can be seen in figure 3.19 and corresponding monochromated EEL spectrum can be seen in figure 3.20. The small pre-edge is located at around 53.7 eV and the main edge at 57.8 eV giving a ΔE of around 4 eV. This is in good agreement with literature for Fe^{3+}[50] [30] [25] [26]. The origin for the Fe $M_{2,3}$ pre-edge and the main edge are the electron transitions from Fe $3p_{1/2}$ and $3p_{3/2}$ states to the unoccupied Fe 3d orbitals. This also confirms that the two edges observed in the energy-loss range 53 - 58 eV in the EEL spectrum of triphylite (fig.3.15) belongs to iron and not lithium.

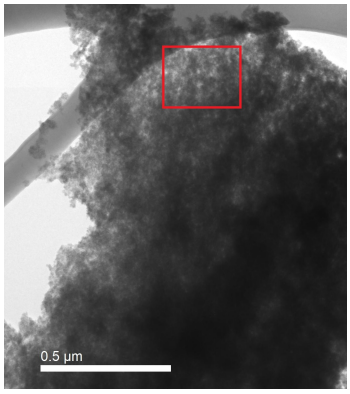

Figure 3.19: Zero-loss filtered TEM image of the investigated Fe_2O_3 material with a red square indicating where the monochromated EELS measurements were done.

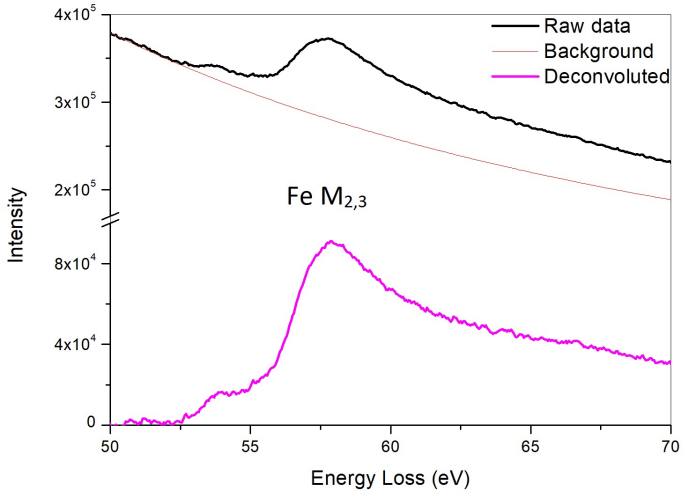

Figure 3.20: Raw monochromated EEL spectrum of the $M_{2,3}$ edge of iron with background and deconvoluted spectrum at 298 K.

3.4 Lithium vanadium phosphate

3.4.1 General information about lithium vanadium phosphate

Lithium vanadium phosphate (LVP) has a chemical composition of ($Li_3V_2(PO_4)_3$) and is used as a cathode material in rechargeable lithium ion batteries. This material is seen as a promising material in future batteries. This is due to the large theoretical specific capacity, high specific energy, high working voltage, good thermodynamic stable structure and low price. Since cathode materials are a determining factor regarding Li-ion batteries, LVP is seen as a promising new cathode material one can use in Li-ion batteries.

The crystal structure of LVP (fig. 3.21b) consists of PO_4 tetrahedra and VO_6 octrahedra that share O atoms and create a 3-D structure. Four VO_6 octahedrons surround one singe PO_4 tetrahedron, while again six PO_4 tetrahedron are surrounding each VO_6 octahedron. Within this structure one can find lithium ions located in holes. Four structural units of $V_2(PO_4)_3$ and three lithium ions placed in crystallographic positions are the building block for the unit cell [49].

In this thesis, a powder LVP was synthesized by a method called the "oxalic acid route" which is a sol-gel method. This method is described in [55], however in this case there was no glucose added as the specimen should not be carbon coated. The precursor samples were sintered at high temperature and a SEM image of this powder can be seen in figure 3.21a. This material will be compared with a lithium vanadium phosphate/carbon (LVP/C) sample synthesized by another sol-gel method [27].

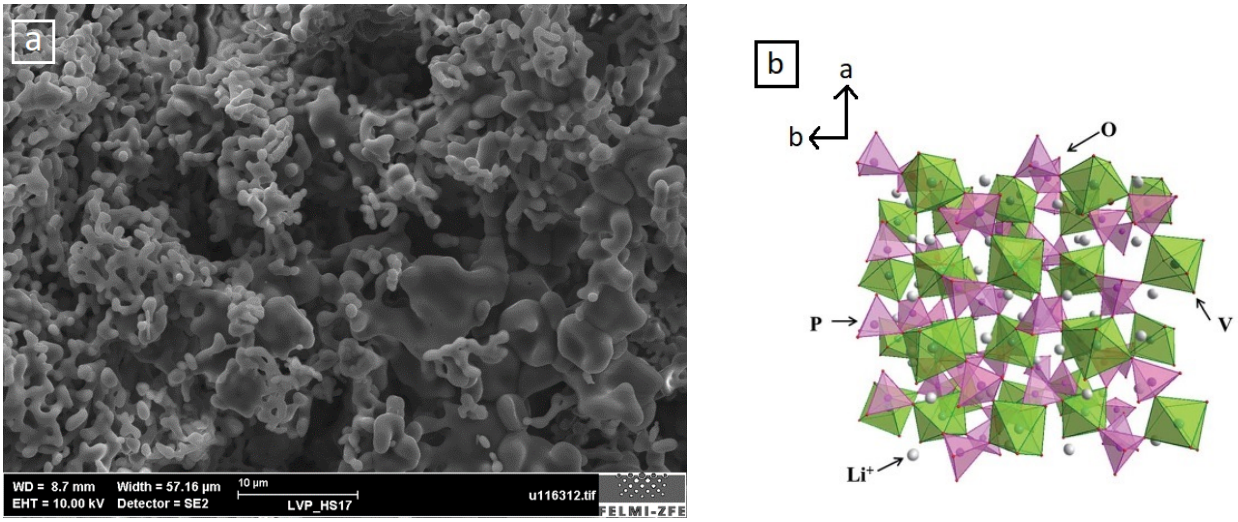

Figure 3.21: (a) SEM image of the LVP sample (by S.Šimić). (b) crystal structure of LVP [15].

3.4.2 EFTEM/TEM investigation

The unfiltered and zero-loss filtered images with the resulting thickness map can be seen in figure 3.22 and an overview of a typical LVP particle is shown in figure 3.23. From this thickness map, the relative thickness t/λ was examined in the marked area where the EELS measurements took place and the average relative thickness was 0.5 t/λ. There are indications that the specimen suffered from beam damage since small circular spots are observed in the locations where the EELS measurements took place. These spots are therefore not included when finding the average relative thickness.

TEM-images of the LVP/C sample are shown in fig.3.24 where G. Haberfehlner recorded EEL spectra from the needle shaped crystals which have been described in literature as LVP/C.

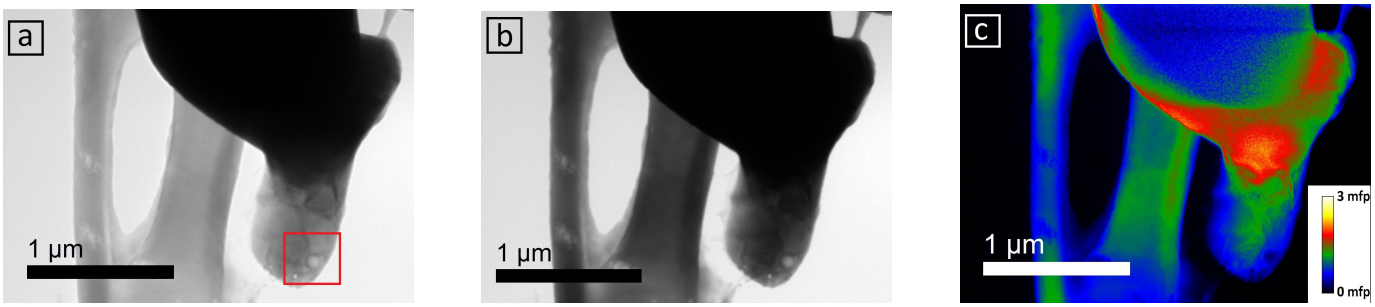

Figure 3.22: (a) Unfiltered TEM image, (b) zero-loss filtered TEM image and (c) resulting relative thickness map.

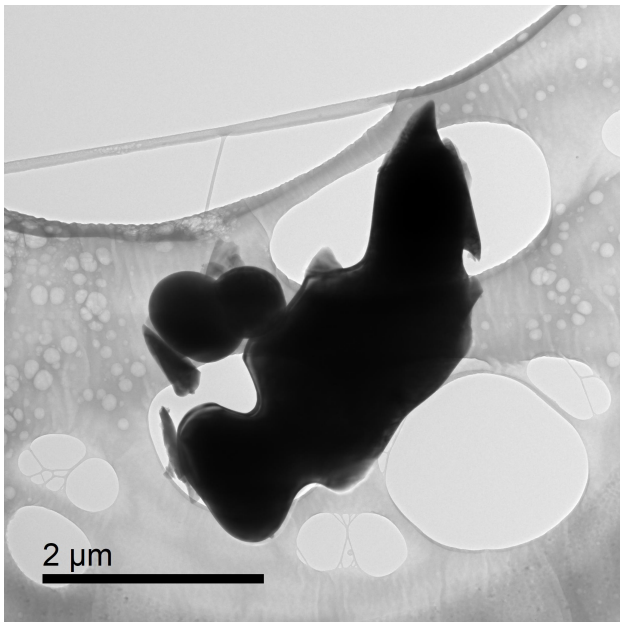

Figure 3.23: General overview unfiltered TEM image of LVP specimen.

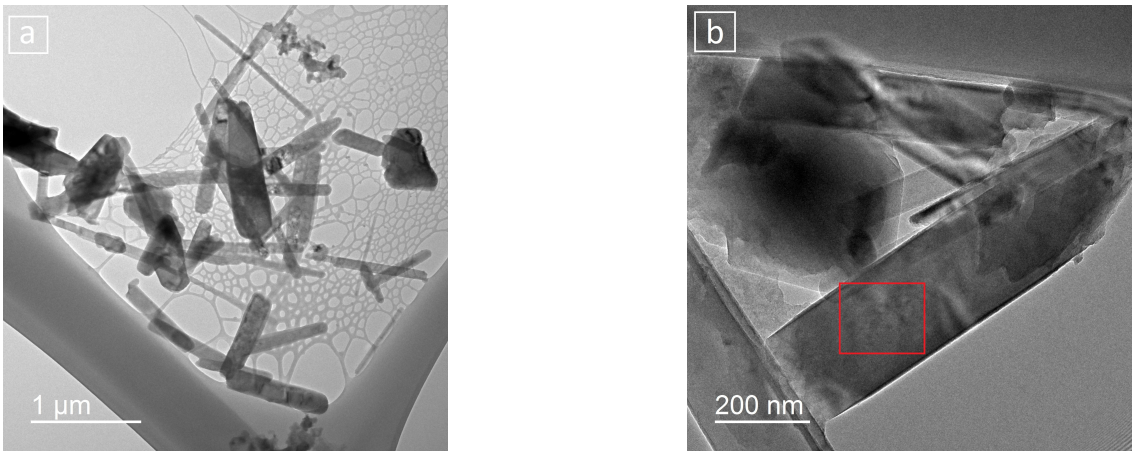

Figure 3.24: (a) Overview zero-loss filtered TEM image of crystals from the LVP/C specimen (b) zero-loss filtered TEM image of where EEL spectra were acquired.

3.4.3 EDX spectroscopy

The LVP sample was also investigated with EDX spectroscopy (fig.3.25). Here C Kα is present at 0.28 keV with V Kα at 4.9 keV, P Kα at 2 keV and the Cu, Co and Fe peaks that are expected when performing EDX in a TEM. This result is also backed up by an EDX SEM.

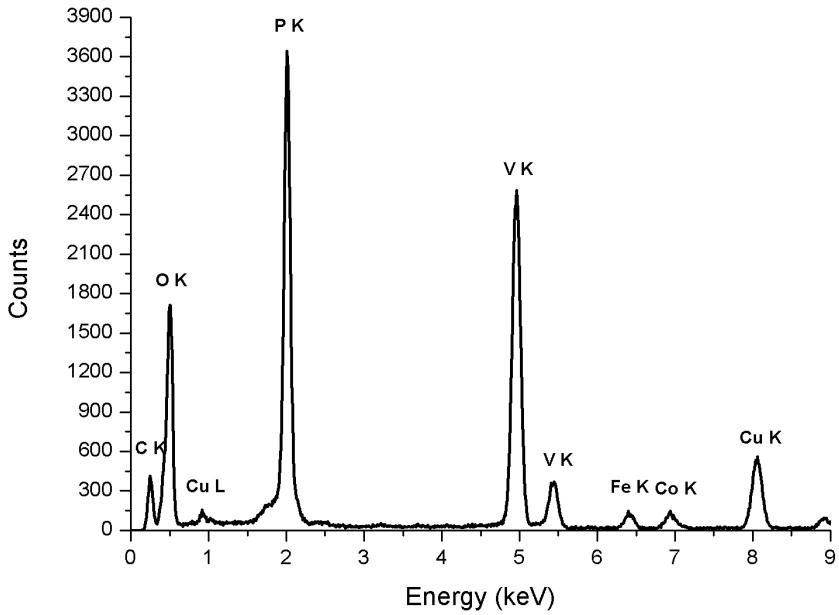

Figure 3.25: EDX spectrum of LVP (including Fe, Co and Cu stray radiation from the TF20) recorded from the specimen region shown in figure 3.22.

3.4.4 Monochromated EEL spectroscopy

The monochromated EEL spectrum (fig. 3.26) with background and spectrum with background substracted of the crystal described as LVP has been recorded from the specimen region shown in fig. 3.22. The V $M_{2,3}$ edge is located at around 40 eV while the Li K edge is at 60 eV. The P $L_{2,3}$ edge is located at 136 eV. Detailed spectra of the edges can be seen in figures 3.28 - 3.30. For a better acquisition of the V $L_{2,3}$ edge and O K edge, the experimental conditions were changed to β = 14.3 mrad and α = 6.06 mrad and the result can be seen in fig. 3.32 . Here the white lines of the V $L_{2,3}$ edge are located at 513 eV and 521 eV, respectively and the O K edge at 532 eV.

The crystals described as LVP/C were investigated using STEM with the following experimental conditions: The convergence angle was set to 19.6 mrad and the collection angle to 20.5 mrad. The EEL spectrum with background and spectrum with background substracted for this LVP/C can be seen in fig. 3.27 and the spectra showing the individual element edges, can be seen in figures 3.29 - 3.31. The spectrum for the O K edge can be seen in 3.33.

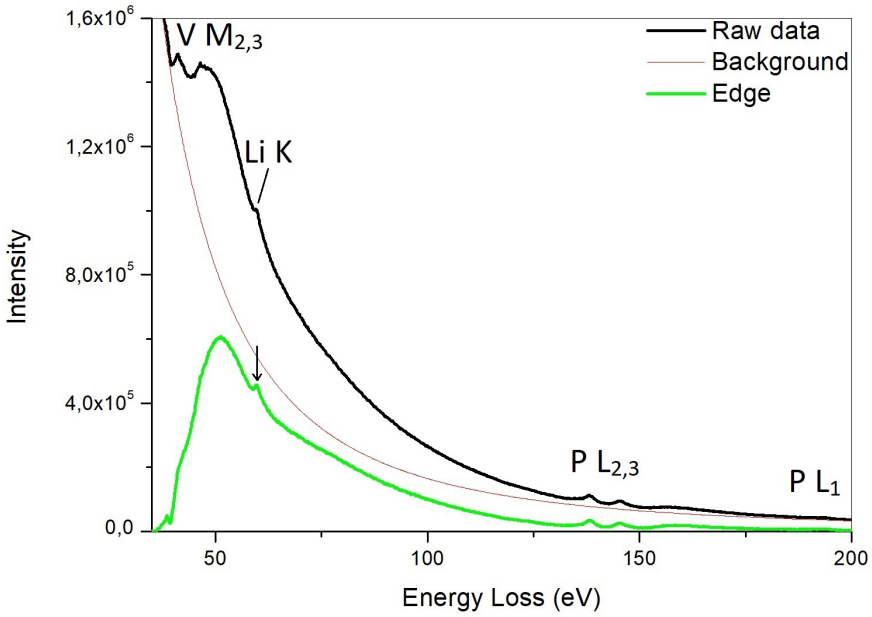

Figure 3.26: Raw monochromated EEL spectrum with background and spectrum with background substracted of the crystal described as LVP from the specimen region shown in figure 3.22.

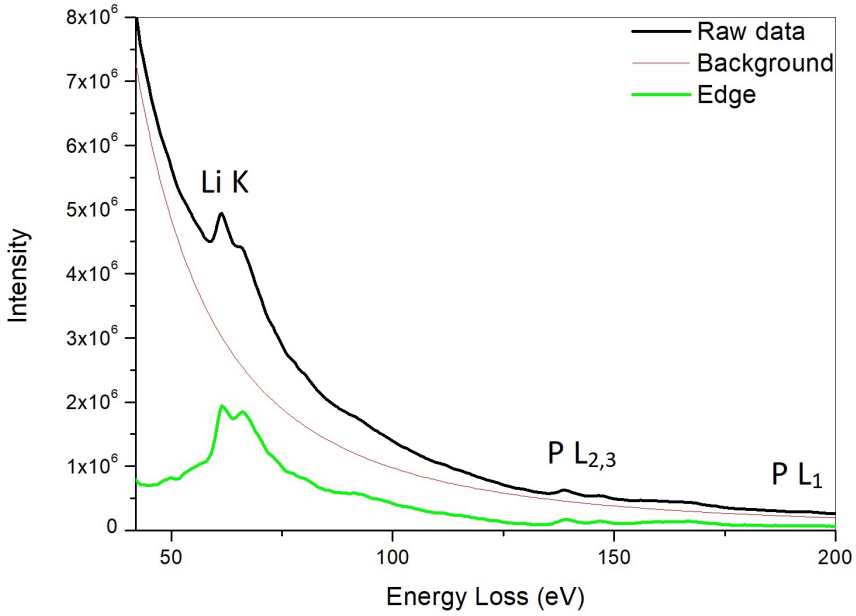

Figure 3.27: EEL spectrum with background and spectrum with background substracted of the crystal described as LVP/C from the specimen region shown in figure 3.24.

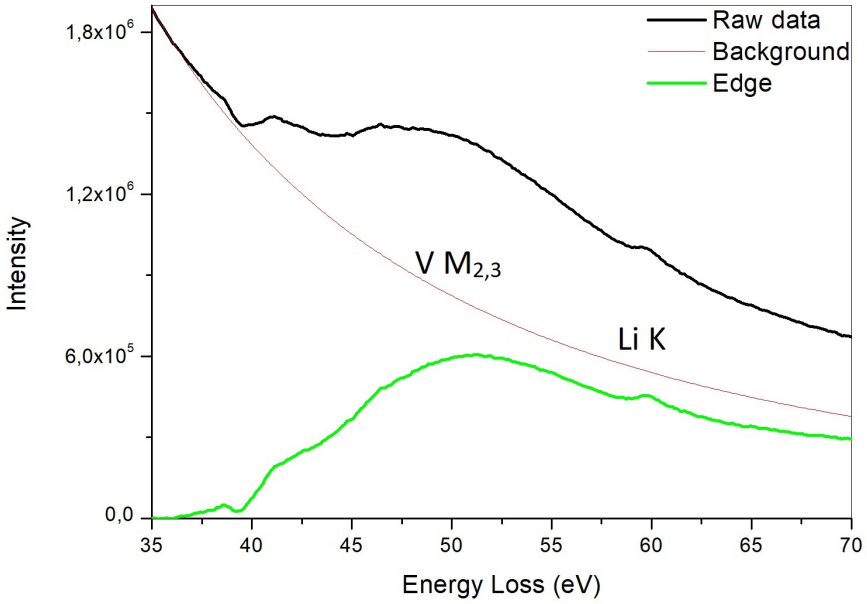

Figure 3.28: $M_{2,3}$ edge of vanadium and K edge of lithium with and without background taken from figure 3.26.

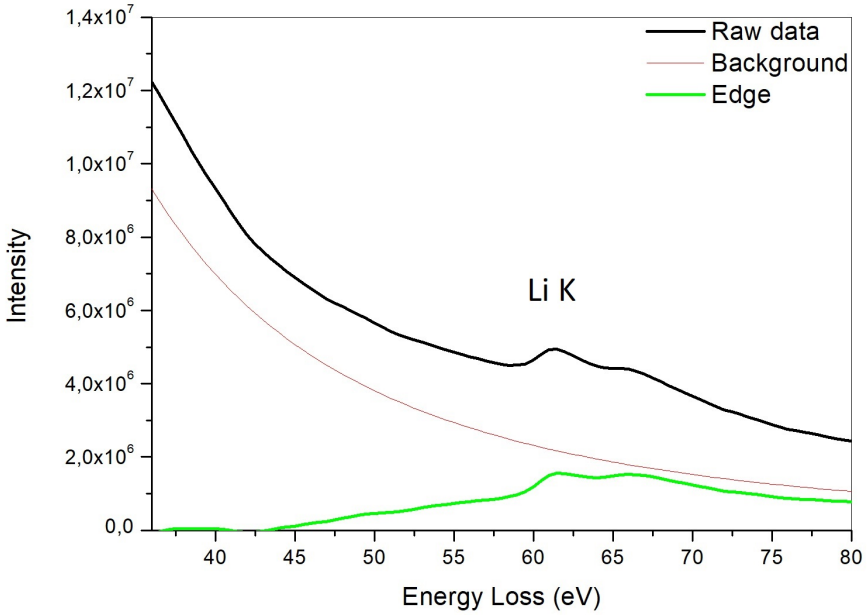

Figure 3.29: K edge of lithium with and without background taken from figure 3.27.

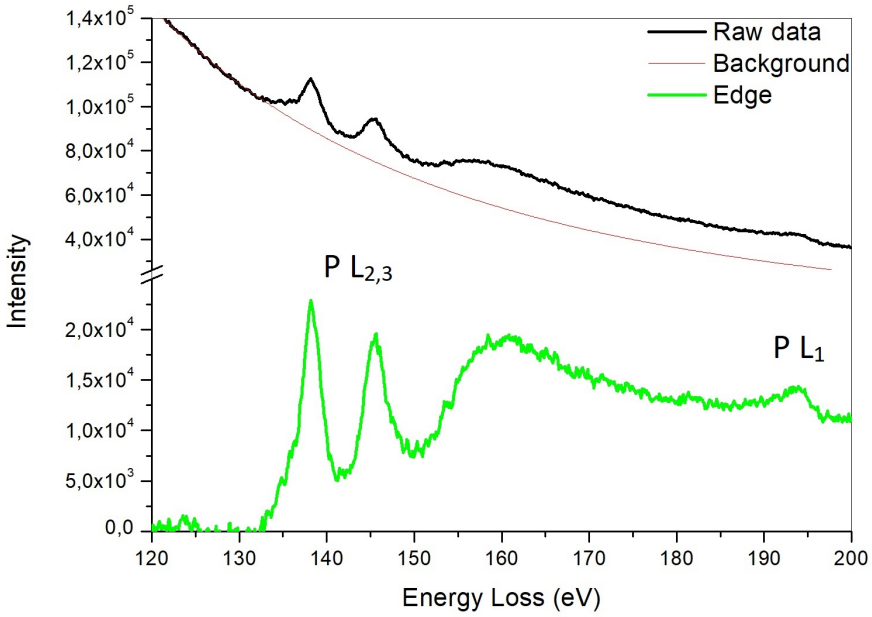

Figure 3.30: $L_{2,3}$ and L_1 edges of phosphorus with and without background taken from figure 3.26.

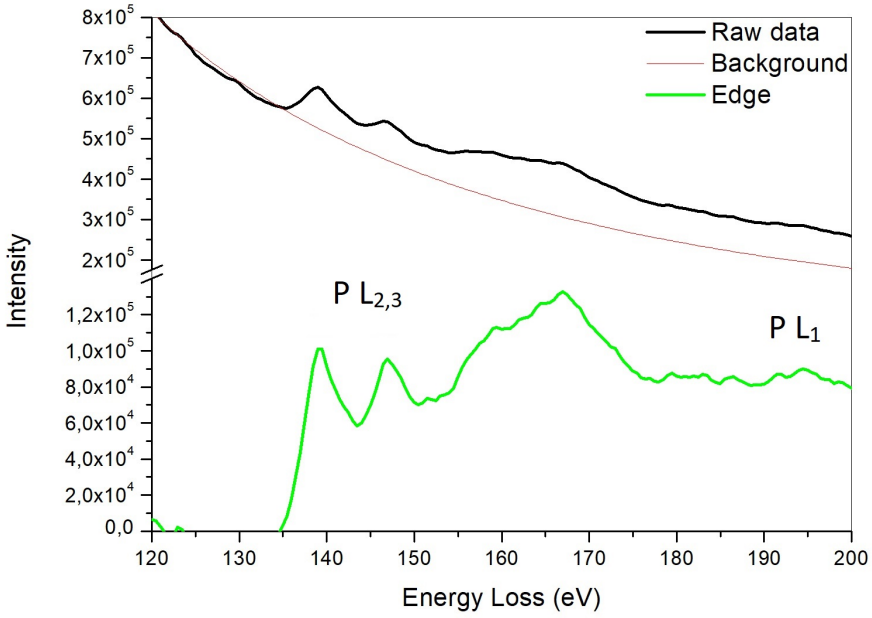

Figure 3.31: $L_{2,3}$ and L_1 edges of phosphorus with and without background taken from figure 3.27.

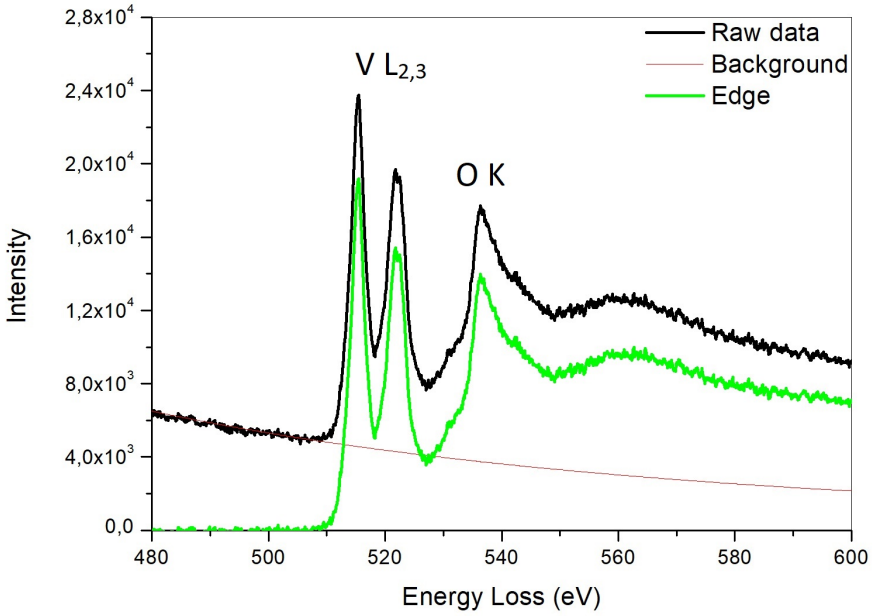

Figure 3.32: $L_{2,3}$ edges of vanadium and K edge of oxygen with and without background with following changes in the experimental conditions: $\beta = 14.3$ mrad and $\alpha = 6.06$ mrad.

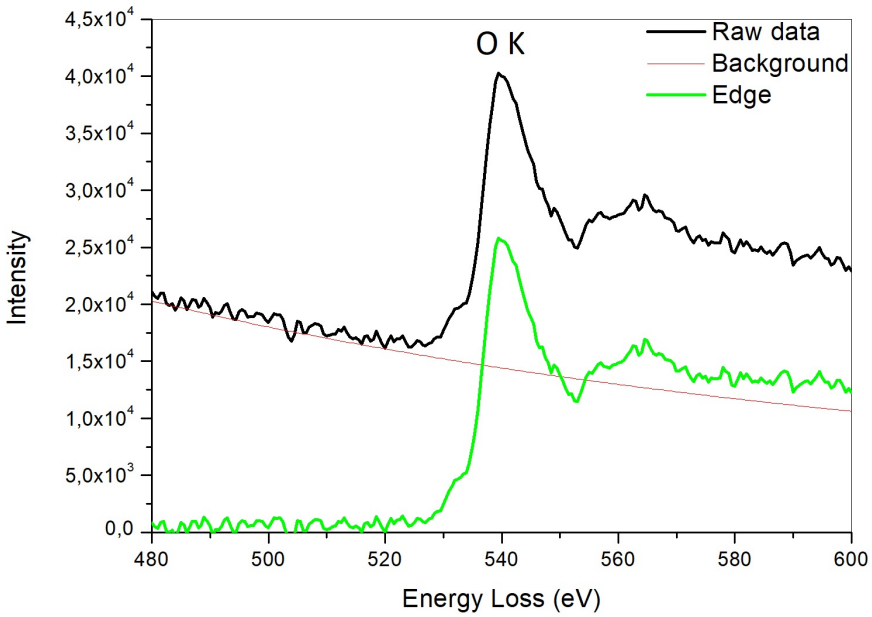

Figure 3.33: K edge of oxygen with and without background taken from figure 3.27.

Chapter 4

Discussion

It is already well known from literature that the micro and nano analysis of lithium is a difficult task [25]. Since X-ray spectroscopy does not give a reliable signal, electron energy-loss spectroscopy (EELS) in the transmission electron microscope is the only method for analysing lithium in materials at high lateral resolution. However, the analysis of lithium by means of EELS is not straight forward and there are some important drawbacks: First one has to control the radiation damage of the specimen during the measurement, which can even lead to loss of lithium and also of crystallinity. Second, the low-loss region gives a high signal, but a very low signal-to-background ratio. Overlapping edges from different elements e.g. the first row of transition metals or the L edges of aluminium and silicon are a problem and therefore it is also very difficult to analyse lithium quantitatively.

In thesis it was tried to have a control on the beam damage and keep this to a minimum by using a cryo holder to cool down the specimen to liquid nitrogen temperature (77K). The experimental procedures were carefully chosen in order to maximize the spectral quality and most EEL spectra have been recorded at high energy-resolution (< 0.6 eV). Besides the qualitative analysis of lithium in different lithium containing materials it was also tried to quantify the spectra by means of different ionization cross section models (comparison of Hartree-Slater and hydrogenic model). Before going in more detail discussing the results achieved in this thesis, some other techniques will be discussed that also can be used for investigating materials which contain lithium:

• Phase contrast imaging in the TEM is a method that can be used in many different applications. This technique exploits changes of refractive index between different materials to differentiate between structures under analysis. When performed using a TEM it is possible to get very high resolution (HR) imaging in the sub-nanometre range and if the TEM is also equipped with a spherical aberration corrector it is even possible to reach atomic resolution (< 100 pm) [11].

• Annular bright field imaging (ABF) in a scanning TEM (STEM) - This technique makes it possible to visualise individual lithium atomic columns simultaneously with heavy elements and if the specimen is thin enough it is also possible to count the number of lithium ions at the column [42]. From this it is theoretically possible to observe movement of lithium ions in the material by taking consecutive ABF images during operation (in-situ ABF observation) [42]. Since the lithium ions are in principle countable, it should be possible to perform semi-quantitative lithium analyses [42].

The problem with this technique is that it is rather limited to qualitative imaging modes and presently it cannot be seen as a reliable technique when it comes to quantification [21]. Other interesting articles about the analysis of lithium using STEM can be found in the special issue of Microscopy [51]. These methods mentioned are interesting but EELS in a TEM/STEM system remains as the presently best method to analyse lithium in materials at a high lateral resolution. There are several publications on Li-containing materials and a comparison of some of these publications have been divided into four parts. Li-oxides, Li-containing phosphates, SEM/TEM studies of Li-V-phosphates and lastly the quantitative EELS analysis of lithium.

4.1 EELS performed on Li-oxides

The publications of Li-oxides provide interesting information regarding EELS, although EELS studies around the Li K edge energy loss range are rare to find. There has been one effort to use in-operando conditions to observe solid-state reactions in Li-ion batteries at high lateral resolution by means of two different types of techniques such as TEM EELS and electron holography [53]. However, the interpretation of these data is not quite straightforward. Studies that include lithium in electrode materials like $LiNi_xMn_yCo_{1-x-y}O_2$ (NMC), cathode materials $Li_{1+x}(NiMnCo)_{1+x}O_2$ and $LiMn_2O_4$ spinel structures, often only contain EELS data on the transition metals and again no focus on the Li K edge [33] [34]. Although STEM-ABF imaging for $Li_4Ti_5O_{12}$ spinel has been performed with the ABF contrast reveals some information about the lithium, but EELS data has only been acquired for the titanium but not for lithium [35]. Other authors used EELS at low resolution on a similar material ($Li_5Ti_4O_{12}$) together with $LiCoO_2$ and $LiMnO_2$ [44]. On the other hand, ELNES structures of the K edge of lithium in lithium oxides and $LiMnO_x$ have been studied in detail [37].

4.2 EELS performed on Li-containing phosphates

There are only a few studies, where Li-containing phosphate materials have been investigated by means of EELS. For example, studies of Li-transition-metal phosphates have been found, where for example LiFe-phosphate has been investigated [46]. In this work lithium has been identified with photo electron spectroscopy (XPS). In another study Li-Ni-phosphate has been investigated by TEM, but no data are provided on lithium [45]. As a natural material triphylite is a rather seldom, but for battery applications artificial $LiFePO_4$/$LiMnPO_4$ powders are increasingly produced and investigated [38]. Therefore, we compared these literature results with our triphylite data and find a good agreement between the spectral features around the K edge of lithium.

4.3 SEM-TEM studies of Li-V-phosphates

Lithium vanadium phosphate is a material that has been more interesting due to its interesting cathode abilities. There are two papers available that have explained the preparation technique including some SEM-TEM investigation of these samples [27] [55]. Samples prepared with both of these techniques have been investigated in this thesis. However, the there was some evidence in this

thesis that one of these papers in fact does not have LVP but Li-phosphate in it. No traces of LVP have been found after a sample was prepared in same way as [27] although doing some modifications to the preparation technique in [55] have been investigated with HR-EELS and LVP has been found.

4.4 Lithium quantification

Lithium quantification in battery materials has been tried in several papers with various results. For example, in [13] $LiCoO_2$ had been quantified with only the ionization cross-section Hartree-Slater model and no experimental conditions for quantification has been mentioned. These authors used a 2 eV energy window for integrating the Li intensity about the edge onset, which is really questionable. Lithiated YBaCuO materials have also been investigated [48]. Here both the ionization cross-section Hartree-Slater and hydrogenic model been used although little information about experimental conditions and quantification. Last paper that will be mentioned regarding quantification is [16]. The Quantification here is done by the ionization cross-section Hartree-Slater model but it is not reproducible nor reliable and there is also a "problem" with Li elemental maps.

4.5 Choice of ionization cross-section model

In the meanwhile, there are many studies showing lithium analysis by means of EELS, but in most cases only qualitative information is available. Just in a few papers it is tried to quantify the Li concentration in Li-containing battery materials, but in most cases data analysis has been only poorly explained and documented. To get a sound basis of how quantification should be performed, well-known Li materials like spodumene and triphylite have been investigated and extended to new materials where the Li concentration has to be confirmed, which is in this thesis is LVP. The main ionization cross-section models focused on in this thesis are the Hartree-Slater model and Hydrogenic model. The hydrogenic model has been proven looking at the results to have limitations when investigating light materials and especially the Li K ionization edge. Suggestions regarding improvement of the hydrogenic model [19] is most likely not included in the GMS software (3.2.0) and therefore not seen as reliable when performing quantification.

4.6 Spodumene

Spodumene is the only material investigated that have previous EELS data and quantification available [25] and can therefore be directly compared with the obtained data in this thesis. The EDX acquired for the spodumene specimen indicate that there are no contaminations in the spodumene crystal and gives also a quick confirmation that Si, Al and O are present in the specimen. For the EELS results, all the ionization edges experience a chemical shift. The Li K, which is due to excitation from 1s state to 2p, is located at around 59 eV instead of 54 eV. The Al $L_{2,3}$, due to excitation of 2p core electron to unfilled states above Fermi level, at 78 eV instead of 73 eV and Si $L_{2,3}$, also due to excitation of 2p core electrons to the empty states, at 105 eV instead of 99 eV. It Is already known that these edges exhibit chemical shifts due to the change of the chemical state from a metal to an insulator, which in this case the difference in band gap shifts the edges to an higher energy loss.

The obtained results are identical to previous data although the resolution has greatly improved that reveal extra peaks, one for the Si $L_{2,3}$ which is the typical shape for SiO_2, also for the Al $L_{2,3}$ which can be compared to the corresponding edge of α-Al_2O_3 (unpublished data by Katharina Riegler, 2009) and by X-ray absorption spectroscopy [40] and the Li K edge has the typical LiF shape [39] instead of just one peak. The energy resolution should, for the previous data, been good enough to observe the two peaks for Li K although the reason why this is not the case is unknown.

4.6.1 Quantification

It has been proven that quantification of especially lithium is more challenging than expected. The up to date version of GMS (3.20.1314.0) uses a model based approach where the background of the whole region from the pre-edge region to the post-edge region is modelled using a Power-law and the signal is modelled based on the ionization cross-section model chosen. This approach does have limitations when the ionization cross-section model does not t the measured edge shape well which was the case when trying to quantify the Li K edge for the spodumene EELS data acquired. Therefore GMS version 2.32.880.0 was used instead. In this version one can manually select a pre-edge region which is fitted with a Power-law and extrapolated to the post-edge region after background subtraction. The net signal of the edge is extracted and integrated over a selected region. This integrated signal is multiplied with the selected ionization cross-section model. In this approach the background is not affected by the cross-section model, but overlapping edges cannot be handled.

Three different spodumene samples with different experimental conditions were quantified using corresponding EEL spectra and then compared. By just changing the cross section model for lithium one can observe a big difference in the atomic ratios as seen in table 3.1. The integrated values (in barn) for the Li K edge ionization cross section for the three different measurements over an interval of 16.7 eV for both models, which is found in table 3.3, show a difference of over 38%. This shows that the ionization cross-section model has to be chosen with care especially when quantifying light elements like lithium and beryllium and even for oxygen K-edge there is a 10% difference between the models as seen in table 3.3.

4.7 Triphylite

There is unfortunately no previous EELS study on triphylite considering the Li K edge and therefore no direct comparison is possible as for spodumene. There are however some studies on $LiFePO_4$ and $LiMnPO_4$ that can be used instead. First EDX both from the TEM and SEM was performed on the specimen to look for both contaminants but also to get an indication regarding Fe/Mn ratio of the specimen using SEM EDX which show close to a 50/50 ratio between these elements.

For the Mn $M_{2,3}$ a small pre-peak at around 47 eV is observed which has not been discussed in several papers except in one [37] and may be interpreted as the transition of Mn $3p_{1/2}$ to the unoccupied Mn 3d orbital referring to the oxidation state of the manganese. The main Mn $M_{2,3}$ is located at 49 eV and is the excitation of Mn 3p core electrons to the d-orbital. The pre-peak at 54 eV is, as proven in other publications, the Fe $M_{2,3}$ edge for the excitation of $3p_{1/2}$ to the unoccupied Fe 3d orbital while the main peak located at 57.5 eV is the excitation of $3p_{3/2}$ to the unoccupied Fe 3d

orbital. The Li K edge is located at 60 eV and is again the excitation from 1s to 2p. The P $L_{2,3}$ and L_1 is due to excitation of 2p core electrons to the empty states and show a near-edge fine structure (ELNES) which is typical for the phosphate anion (PO_4^{3-}) [24]. Due to the overlap of the Mn $M_{2,3}$, the Fe $M_{2,3}$ and the Li K edges, quantification performed like on spodumene is impossible. The only solution would be to record edges of the corresponding oxides [25] or simulate the edges [31] and finally fitting them to the triphylite spectrum by using an MLLS approach.

4.8 Lithium vanadium phosphate

As in the case for triphylite, no EELS study has been performed on LVP for the K edge of lithium and the $M_{2,3}$ edge of vanadium so a direct comparison is not possible. The EDX spectra acquired for the LVP specimen indicate that there are no contaminations in the LVP crystals and also give a quick confirmation that only vanadium and phosphorous are present. Some interesting features are observed in the acquired EELS data. The vanadium $M_{2,3}$ edge is quite broad and was first believed in this thesis to be just a Plasmon peak due to thickness and not an edge. The lithium K edge is also different from the two previous minerals since only one peak is observed and not two as in the previous cases. The phosphorus also may have a pre-ionization edge which is not present in the other minerals.

The EELS data from the LVP acquired in this thesis were compared to previous EELS investigations on an LVP sample produced by a sol-gel method with carbon (LVP/C) [27]. Low-loss EELS can be seen in fig.3.27, the Li K edge can be seen in figure 3.29 and the P $L_{2,3}$ edge in fig.3.31, respectively. The main difference between these EEL spectra is that for LVP we are able to identify a peak before the Li K edge, which cannot be seen in LVP/C. This peak is due to the V $M_{2,3}$ edge and therefore we immediately know that the LVP/C phase does not include a higher concentration of vanadium. The Li K edge for the LVP/C has the characteristic LiF shape and not just a single peak as seen in fig.3.28. These findings open the question if both samples are really lithium vanadium phosphates which has been already questioned by Georg Haberfehlner in 2017, when he found that the needle shaped crystals in LVP/C do not contain vanadium.

Since the $M_{2,3}$ edge of vanadium is not the ultimate proof for vanadium, it was necessary to concentrate on the vanadium $L_{2,3}$ edge. This should give a clear indication if there is any trace of vanadium and give stronger evidence that the peak observed at around 50 eV is in fact the vanadium $M_{2,3}$ edge. The EEL spectrum for LVP is shown in fig.3.32. Here one can see the oxygen K edge above 532 eV overlapping with the vanadium $L_{2,3}$ edge starting at 513 eV. At the onset of the vanadium edge we find the typical "white lines" and it is already known that the total L_3 and L_2 intensity decreases with increasing occupancy of the d-band and that the L_3/L_2 intensity ratios strongly depend on the valence state of the corresponding transition element [16]. However, the EEL spectrum of LVP/C recorded by Georg Haberfehlner (fig.3.33) does not show any vanadium and consequently we have the ultimate proof that the needle shaped crystals in the LVP/C sample are lithium phosphate crystals. Therefore, we are able to say that the crystals first described by [27] are not lithium vanadium phosphate but only lithium phosphate. This phase should not influence the electrochemical properties of the LVP preparations.

Chapter 5

Conclusion

In this thesis it has been proven that considerable steps need to be taken to perform good qualitative analysis of lithium. To have a better control on the beam damage, a cryo holder needs to be used to cool down the specimen with liquid nitrogen (77K) and it is essential that the experimental procedures are carefully chosen to maximize the spectral quality. If the specimen is exposed to the electron beam for a longer time, it has been proven that the lithium concentration will decrease and the specimen will lose its crystallinity.

The monochromated EEL spectrum of spodumene, is the first one which has been recorded with high energy resolution well below 0.6 eV. This spectrum show detailed near-edge structures where one can find information about the chemical coordination for the Li-ion and the spin-orbit splitting at the $L_{2,3}$ ionization edges for α-Al_2O_3 and α-SiO_2. A more thorough quantification of spodumene using both the Hartree-Slater and hydrogenic model have proven the limitation for the hydrogenic model where the ionization cross section values between these models show differences of up to 38 %.

The monochromated EEL spectrum of triphylite is the only spectrum in literature and is recorded with high energy resolution ($<$0.6 eV) where one can observe the main strong Mn $M_{2,3}$ edge, the Fe $M_{2,3}$ edges, where the pre-peak was confirmed to be due to the oxidation state of iron by EELS investigation of an iron oxide, the Li K edge with the typical "saw tooth" shape and lastly the P L edges which show a typical near-edge fine structure one can find for the phosphate anion PO_4^{3-}.

A monochromated high energy resolution EEL spectrum well below 0.6 eV for lithium vanadium phosphate has also been recorded and is also the first spectrum that has been recorded for this crystal. Here the $M_{2,3}$ edge for vanadium, a weak Li K edge which only has one peak and not the typical "saw tooth" shape followed by the P $L_{2.3}$ edge with the typical near-edge fine structure one can find for the phosphate anion PO_4^{3-} is observed. A confirmation of the presence of vanadium is strengthened by EELS of the vanadium $L_{2,3}$ edge and EDX-spectroscopy. This EELS investigation of the described LVP crystal shows that the described LVP/C which the LVP spectrum has been compared with, in reality is a Li-phosphate and not LVP/C.

List of Tables

List of Figures

Bibliography

[1] Basics of x-ray. URL https://miac.unibas.ch/PMI/01-BasicsOfXray.html#(17).

[2] Microscopy and analysis. URL https://microscopy-analysis.com/editorials/editorial-listings/how-optimize-your-eels-experiments-adjusting-collection-angle-your.

[3] FEI Tecnai F20. URL https://www.felmi-zfe.at/instrumentation/tem/fei-tecnai-f20/.

[4] Spodumene. URL https://geology.com/minerals/spodumene.shtml.

[5] EELS, Jan 1970. URL http://www.gatan.com/techniques/eels.

[6] Triphylin, May 2005. URL https://roempp.thieme.de/roempp4.0/do/data/RD-20-03081#Literatur.

[7] Energy-filtered transmission electron microscopy (EFTEM), Feb 2015. URL http://www.microscopy.ethz.ch/GIF.htm.

[8] Thickness map, Mar 2016. URL http://www.eels.info/how/eftem/workflow/thickness-map.

[9] Practical electron microscopy and database, 2018. URL www.globalsino.com/EM/.

[10] Collection angle considerations, Jan 2019. URL http://www.eels.info/how/getting-started/collection-angle-considerations.

[11] Phase-contrast imaging, Feb 2019. URL https://en.wikipedia.org/wiki/Phase-contrast_imaging.

[12] Spodumene, Jan 2019. URL https://en.wikipedia.org/wiki/Spodumene.

[13] Tomoki Akita and Noboru Taguchi. Practical analysis of Li distribution by EELS. *Surface and Interface Analysis*, 48(11):1226–1230, 2016. doi: 10.1002/sia.6082.

[14] Rik Brydson. *Electron energy loss spectroscopy*. Taylor & Francis, 2006.

[15] Renjie Chen, Jingning Lai, Yuejiao Li, Meiling Cao, Shi Chen, and Feng Wu. β-Cyclodextrin coated lithium vanadium phosphate as novel cathode material for lithium ion batteries. *RSC Advances*, 6(105):103364–103371, Oct 2016. doi: 10.1039/c6ra22400h.

[16] F. Cosandey, D. Su, M. Sina, N. Pereira, and G.g. Amatucci. Fe valence determination and Li elemental distribution in lithiated $FeO_{0.7}F_{1.3}$/C nanocomposite battery materials by electron energy loss spectroscopy (EELS). *Micron*, 43(1):22–29, May 2012. doi: 10.1016/j.micron.2011.05.009.

[17] R.f. Egerton. Formulae for light-element micro analysis by electron energy-loss spectrometry. *Ultramicroscopy*, 3:243–251, 1978. doi: 10.1016/s0304-3991(78)80031-x.

[18] R.f. Egerton. K-shell ionization cross-sections for use in microanalysis. *Ultramicroscopy*, 4(2):169–179, 1979. doi: 10.1016/s0304-3991(79)90157-8.

[19] R.f. Egerton. Improvement of the hydrogenic model to give more accurate values of K-shell ionization cross sections. *Ultramicroscopy*, 63(1):11–13, Apr 1996. doi: 10.1016/0304-3991(96)00034-4.

[20] R.F Egerton. *Electron Energy-Loss Spectroscopy in the Electron Microscope*. Springer US, 2011.

[21] Scott David Findlay, Rong Huang, Ryo Ishikawa, Naoya Shibata, and Yuichi Ikuhara. Direct visualization of lithium via annular bright field scanning transmission electron microscopy: a review. *Microscopy*, 2016. doi: 10.1093/jmicro/dfw041.

[22] S. Geller and J. L. Durand. Refinement of the structure of $LiMnPO_4$. *Acta Crystallographica*, 13(4):325–331, 1960. doi: 10.1107/s0365110x60002521.

[23] Ferdinand Hofer. Determination of inner-shell cross-sections for EELS-quantification. *Microscopy Microanalysis Microstructures*, 2(2-3):215–230, Apr 1991. doi: 10.1051/mmm:0199100202-3021500.

[24] Ferdinand Hofer and Peter Golob. New examples for near-edge fine structures in electron energy loss spectroscopy. *Ultramicroscopy*, 21(4):379–383, 1987. doi: 10.1016/0304-3991(87)90036-2.

[25] Ferdinand Hofer and Gerald Kothleitner. Quantitative microanalysis using electron energy-loss spectrometry. I. Li and Be in oxides. *Microscopy Microanalysis Microstructures*, 4(6):539–560, Dec 1993. doi: 10.1051/mmm:0199300406053900.

[26] Ferdinand Hofer and Peter Wilhelm. EELS microanalysis of the elements Ca to Cu using M_{23} edges. *Ultramicroscopy*, 49(1-4):189–197, Aug 1993. doi: 10.1016/0304-3991(93)90225-m.

[27] Caixia Huang, Dandan Chen, Yiyin Huang, and Yonglang Guo. Sol–gel synthesis of $Li_3V_2(PO_4)_3$/C cathode materials with high electrical conductivity. *Electrochimica Acta*, 100:1–9, Mar 2013. doi: 10.1016/j.electacta.2013.03.073.

[28] Alexander A. Kaminskii, Ladislav Bohatý, Eugen Libowitzky, Hanjo Rhee, Oliver Lux, Hans J. Eichler, Reiner Kleinschrodt, Hitoki Yoneda, Akira Shirakawa, Petra Becker, and et al. Spodumene, α-$LiAlSi_2o_6$ – A new natural SRS-active crystal with three $\chi^{(3)}$-promoting vibrational modes. *Optical Materials*, 78:235–246, Feb 2018. doi: 10.1016/j.optmat.2018.02.022.

[29] Koji Kimoto. Practical aspects of monochromators developed for transmission electron microscopy. *Microscopy*, 63(5):337–344, 2014. doi: 10.1093/jmicro/dfu027.

[30] Shunsuke Kobayashi, Craig A. J. Fisher, Akihide Kuwabara, Yoshio Ukyo, and Yuichi Ikuhara. Quantitative analysis of Li distributions in battery material $Li_{1-x}FePO_4$ using Fe $M_{2,3}$-edge and valence electron energy loss spectra. *Journal of Electron Microscopy*, 66(4):254–260, 2017. doi: 10.1093/jmicro/dfx012.

[31] Lukas Konrad, Haishuang Zhao, Christian Gspan, John Rehr, Ute Kolb, Martina Lattemann, and Gerald Kothleitner. A consistent path for phase determination based on transmission electron microscopy techniques and supporting simulations. *Micron*, 115:41–49, 2018. doi: 10.1016/j.micron.2018.08.007.

[32] Frank Krumeich. Properties of electrons, their interactions with matter ... URL `http://www.microscopy.ethz.ch/downloads/Interactions.pdf`.

[33] Hanshuo Liu and Gianluigi A. Botton. Understanding the Chemical and Relevant Phase Evolutions of Lithium-Based Electrode Materials Using Atomic-Resolution Electron Energy Loss Spectroscopy. *Microscopy and Microanalysis*, 24(S1):1520–1521, 2018. doi: 10.1017/s1431927618008085.

[34] Hanshuo Liu, Matthieu Bugnet, Matteo Z. Tessaro, Kristopher J. Harris, Mark J. R. Dunham, Meng Jiang, Gillian R. Goward, and Gianluigi A. Botton. Spatially resolved surface valence gradient and structural transformation of lithium transition metal oxides in lithium-ion batteries. *Physical Chemistry Chemical Physics*, 18(42):29064–29075, Aug 2016. doi: 10.1039/c6cp05262b.

[35] Xia Lu, Liang Zhao, Xiaoqing He, Ruijuan Xiao, Lin Gu, Yong-Sheng Hu, Hong Li, Zhaoxiang Wang, Xiaofeng Duan, Liquan Chen, and et al. Lithium storage in $Li_4Ti_5O_{12}$ Spinel: The Full Static Picture from Electron Microscopy. *Advanced Materials*, 24(24):3233–3238, 2012. doi: 10.1002/adma.201200450.

[36] Naresh Marturi. Vision and visual servoing for nanomanipulation and nanocharacterization in scanning electron microscope. 11 2013.

[37] V. Mauchamp, F. Boucher, G. Ouvrard, and P. Moreau. Ab initiosimulation of the electron energy-loss near-edge structures at the Li K edge in Li,Li_2O, and $LiMn_2O_4$. *Physical Review B*, 74(11), 2006. doi: 10.1103/physrevb.74.115106.

[38] P. Moreau and F. Boucher. Revisiting lithium K and iron $M_{2,3}$ edge superimposition: The case of lithium battery material lifepo4. *Micron*, 43(1):16–21, May 2012. doi: 10.1016/j.micron.2011.05.008.

[39] Shunsuke Muto and Kazuyoshi Tatsumi. Detection of local chemical states of lithium and their spatial mapping by scanning transmission electron microscopy, electron energy-loss spectroscopy and hyperspectral image analysis. *Microscopy*, 2016. doi: 10.1093/jmicro/dfw038.

[40] O'brien, Jia W. L., Dong, Callcott, Rubensson, Mueller, Ederer, and D. L. Intermediate coupling in L_2-L_3 core excitons of MgO, Al_2O_3, and SiO_2, Jul 1991. URL `http://adsabs.harvard.edu/abs/1991PhRvB..44.10130`.

[41] Denis Ar On, Andrej Zorko, Robert Dominko, and Zvonko Jagli i. A comparative study of magnetic properties of $LiFePO_4$ and $LiMnPO_4$. *Journal of Physics: Condensed Matter*, 16(30): 5531–5548, 2004. doi: 10.1088/0953-8984/16/30/014.

[42] Yoshifumi Oshima, Soyeon Lee, and Kunio Takayanagi. Visualization of lithium ions by annular bright field imaging. *Microscopy*, 2016. doi: 10.1093/jmicro/dfw098.

[43] Thomas P.J. and Midgley P.A. Image-spectroscopy–II. The removal of plural scattering from extended energy-filtered series by Fourier deconvolution. *Ultramicroscopy*, 88(3):187–194, Sep 2001. doi: 10.1016/S0304-3991(01)00078-X.

[44] Anuj Pokle, João Coelho, Eva Macguire, Clive Downing, Patrick Casey, Cormac Mcguinness, and Valeria Nicolosi. EELS Probing of lithium based 2-D battery compounds processed by liquid phase exfoliation. *European Microscopy Congress 2016: Proceedings*, page 851–852, 2016. doi: 10.1002/9783527808465.emc2016.5853.

[45] C. V. Ramana, A. Ait-Salah, S. Utsunomiya, U. Becker, A. Mauger, F. Gendron, and C. M. Julien. Structural Characteristics of Lithium Nickel Phosphate Studied Using Analytical Electron Microscopy and Raman Spectroscopy. *Chemistry of Materials*, 18(16):3788–3794, Jun 2006. doi: 10.1021/cm061137c.

[46] C. V. Ramana, A. Ait-Salah, S. Utsunomiya, J.-F. Morhange, A. Mauger, F. Gendron, and C. M. Julien. Spectroscopic and Chemical Imaging Analysis of Lithium Iron Triphosphate. *The Journal of Physical Chemistry C*, 111(2):1049–1054, Oct 2007. doi: 10.1021/jp065072c.

[47] Peter Rez. Cross-sections for energy loss spectrometry. *Ultramicroscopy*, 9(3):283–287, 1982. doi: 10.1016/0304-3991(82)90213-3.

[48] M.a. Señarís-Rodríguez, H. Gu, C. Colliex, and M.a. Alario-Franco. The microstructure, local chemical and electronic properties of lithiated YBaCuO materials investigated with HREM, EDX and EELS techniques. *Journal of Physics and Chemistry of Solids*, 58(4):597–606, Feb 1997. doi: 10.1016/s0022-3697(96)00173-4.

[49] Du Tao, Shengping Wang, Yongchao Liu, Yu Dai, Jingxian Yu, and Xinrong Lei. Cheminform abstract: Lithium Vanadium Phosphate as Cathode Material for Lithium Ion Batteries. *ChemInform*, 46(33), 2015. doi: 10.1002/chin.201533255.

[50] Josh Vura-Weis, Chang-Ming Jiang, Chong Liu, Hanwei Gao, J. Matthew Lucas, Frank M. F. De Groot, Peidong Yang, A. Paul Alivisatos, and Stephen R. Leone. Femtosecond $M_{2,3}$-edge spectroscopy of transition-metal oxides: Photoinduced oxidation state change in α-Fe_2O_3. *The Journal of Physical Chemistry Letters*, 4(21):3667–3671, 2013. doi: 10.1021/jz401997d.

[51] Yuren Wen, Tongtong Shang, and Lin Gu. Analytical ABF-STEM imaging of Li ions in rechargeable batteries. *Microscopy*, 2016. doi: 10.1093/jmicro/dfw100.

[52] David B. Williams and C. Barry Carter. *Transmission electron microscopy a textbook for materials science*. Plenum Press, 2009.

[53] Kazuo Yamamoto, Yasutoshi Iriyama, and Tsukasa Hirayama. Operando observations of solid-state electrochemical reactions in li-ion batteries by spatially resolved tem eels and electron holography. *Microscopy*, 2016. doi: 10.1093/jmicro/dfw106.

[54] Karim Zaghib, Alain Mauger, and Christian M. Julien. Olivine-Based Cathode Materials. *Rechargeable Batteries Green Energy and Technology*, page 25–65, Jun 2015. doi: 10.1007/978-3-319-15458-9_2.

[55] Lu-Lu Zhang, Ying Li, Gang Peng, Zhao-Hui Wang, Jun Ma, Wu-Xing Zhang, Xian-Luo Hu, and Yun-Hui Huang. High-performance $Li_3V_2(PO_4)_3$/C cathode materials prepared via a sol–gel route with double carbon sources. *Journal of Alloys and Compounds*, 513:414–419, Feb 2012. doi: 10.1016/j.jallcom.2011.10.059.